Front. Phys. China (2006) 4: 468－489
DOI 10.1007/s11467-006-0042-8

REVIEW ARTICLE

ZENG Jiao-long, JIN Feng-tao, YUAN Jian-min

Radiative opacity of plasmas studied by detailed term (level) accounting approaches

Abstract Detailed term and level accounting (DTA and DLA) schemes have been developed to calculate the spectrally resolved and Rosseland and Planck mean opacities of plasmas in local thermodynamic equilibrium. Various physical effects, such as configuration interaction effect (including core-valence electron correlations effect and relativistic effect), detailed line width effect (including the line saturation effect), etc., on the opacity of plasmas have been investigated in detail. Some of these physical effects are less capable or even impossible to be taken into account by statistical models such as unresolved transition arrays, super-transition-array or average atom models. Our detailed model can obtain accurate opacity of plasmas. Using this model, we have systematically investigated the radiative opacities of low, medium and high-Z plasmas under different conditions of temperature and density. For example, for aluminum plasma, in the X-ray region, we demonstrated the effects of autoionization resonance broadening on the opacity for the first time. Furthermore, the relativistic effects play an important role on the opacity as well. Our results are in good agreement with other theoretical ones although better agreement can be obtained after the effects of autoionization resonance broadening and relativity have been considered. Our results also show that the modelling of the opacity is very complicated, since too many physical effects influence the accuracy of opacity.

For medium and high-Z plasmas, however, there are systematic discrepancies unexplained so far between the theoretical and experimental opacities. Here, the theoretical opacities are mainly obtained by statistical models. To clarify the discrepancies, efforts from both sides are needed. From the viewpoint of theory, however, a DLA method, in which various physical effects can be taken into account, should be useful in resolving the difference. Taking gold plasma as an example, we studied in detail the effects of core-valence electron correlation and line width on the opacity. Our DLA results correctly explained, for the first time, the relative intensity of the two strong absorption peaks located near the photon energy of 70 and 80 eV, which was experimentally observed by Eidmann *et al*. [Europhys. Lett., 1998, 44: 459].

Keywords radiative opacity, plasma, detailed term (level) accounting

PACS numbers 52.50.Nr, 52.20.-j, 32.80.Hd

1 Introduction

The radiative opacity of high temperature plasmas have been of great utility in the study of inertial confinement fusion (ICF) [1, 2], stellar physics [3] and X-ray lasers. Experimental and theoretical determinations of the radiative opacity have long been of interest. This interest is mainly due to the urgent need of the radiative opacity for practical applications, fusion research and plasma diagnostics. Moreover, the Rosseland opacity is a crucial parameter in the study of radiative transfer of astrophysical and laboratory plasmas. On the other hand, one can get important information on the plasma properties, such as temperature, density and different ionization stage distribution by combining the spectrally resolved opacity with the simulation results of radiation-hydrodynamics. In short, the radiative opacity plays important roles in many research fields. The National Ignition Facility (NIF), which will be completed in 2010, emphasizes the importance of opacity measurement.

During the last two decades, great progress has been made in experimental measurements of the radiative opacity of high temperature plasmas. A detailed review of the experimental progresses is beyond this work. One can find more details in a recent PhD thesis [5]. To have a peer view,

ZENG Jiao-long, JIN Feng-tao, YUAN Jian-min (✉)
Department of Physics, National University of Defense Technology, Changsha 410073, China
E-mail: jmyuan@nudt.edu.cn

Received August 12, 2006

we take aluminum plasma as an example. In the past two decades, aluminum plasmas have been of particular experimental concern. Most of the experimental researches on Al plasmas were done in the X-ray region where the spectral range is at $h\nu \gtrsim 1$ keV. Davidson *et al*. [6, 7] measured the transmis-sion of X-rays from an external source of known intensity through an aluminum plasma that was created by indirect laser irradiation. Local thermodynamic equilibrium (LTE) was obtained in their experiment and its X-ray absorption properties were measured. The experiments yielded plasma of about 40 eV temperature and 0.005 of solid density with the aluminum ions having 4－8 bound electrons. The measured transmission spectrum is in the photon energy range of 1480－1580 eV corresponding to the inner-shell excitations from 1s to 2p orbital. Perry *et al*. [8] made a similar experiment, but the experimental condition was slightly modified. AlXII through AlVIII had been made in a laser-heated slab plasma at the measured temperature and density of 58 ± 4 eV and 0.020 ± 0.007 g $\cdot$ cm^{-3}. Perry *et al*. [9] also made a radiation transfer experiment by using the K-shell absorption spectra and Iglesias *et al*. [10] had done detailed analysis of the experiment. Besides the direct opacity measurements of Al plasma, a lot of experiments (see, for example, Refs. [11, 12]) had used the X-ray transmission spectrum of Al as temperature and density diagnostics. Compared with the spectral range $h\nu \gtrsim 1$ keV, fewer researches had been carried out on Al plasmas covering the range $h\nu \lesssim 1$ keV. However, it is this spectral range which determines the Rosseland and Planck mean opacities under present typical plasma conditions (temperatures of a few tens of eV). To our knowledge, only a few experimental studies [13, 14] were carried out in this spectral range for Al plasmas. Winhart *et al*. [13, 14] measured the spectrally resolved opacities (through transmission) of aluminum in the energy range of 70 eV to 280 eV at a typical temperature and density of about 20 eV and 0.01 g $\cdot$ cm^{-3}, respectively. LTE was obtained in their experiment.

In spite of the fact that vast advances have been made in the opacity measurements, they are still far away from satisfying practical applications. The main role of experimental investigations should be verifying the validity of theoretical models. In practical applications, one usually needs Rosseland and Planck mean opacities. To obtain these mean opacities, in principle, one needs to measure spectrally resolved opacities in the whole spectral range (from zero to infinity for frequency or photon energy). At present, such an experimental measure is hard to achieve. Therefore, in most practical applications, the radiative opacity is obtained by theoretical methods. Theoretical effort can be dated back to 1923, when Kramers [15] obtained the classic hydrogenic free-free and bound-free absorption cross sections.

In the early stages, theoretical models for the calculations of radiative opacity are based on the statistical methods. Green [16] first published the paper of the self-consistent average atom (AA) model to calculate the opacity. Bauche *et al*. [17,18] proposed the model of unresolved transition arrays (UTA), especially for the heavy atoms' spectra and opacity. Bar-Shalom *et al*. [19] noticed that lines of different transition arrays are unresolved and therefore proposed a model of Super-transition-array (STA). The AA, UTA and STA models are statistical ones because statistical treatment is required to deal with the intensity distribution and line width.

The models of detailed term accounting (DTA) and detailed level accounting (DLA) are most suitable for obtaining detailed spectrally resolved opacity. Theoretical modelling for the radiative opacity of high temperature plasmas requires a lot of information such as atomic data, state populations, spectral line shapes and plasma conditions. As for the spectral line shapes, there are several broadening mechanisms, such as natural width, autoionizing resonance and collision broadening and Doppler broadening. In principle, all these broadening mechanisms should be considered in a complete treatment, while in practice only the main factors are considered. Therefore, the modelling of DTA and DLA is very complex, not only because one has to obtain a great number of atomic data and to take many different physical effects on the atomic data into account, but also because there are many unpredictable factors to consider.

Up to now, DTA and DLA have achieved great success in predicting the opacity of low-Z plasmas such as Al. Abdallah and Clark [20] first carried out detailed calculation on the 1s－ 2p opacity of aluminum plasmas using the DTA model. Their calculations treated approximately the K-shell excited states as discrete ones and used the Gaussian profile for the spectral line shape with Doppler width being considered. A configuration interaction (CI) calculation on the opacity of Al plasmas was carried out by Iglesias *et al*. [21] with orbital wave functions computed using the Dirac-Hatree-Slater (DHS) method. They used the Voigt profile including electron collision broadening and Doppler widths. Actually, these K-shell excited states are well above the ionization threshold and the photo-excitations of a 1s electron to the 2p orbital are autoionization processes. We [22] carried out a detailed calculation which treats the 1s－2p transitions as autoionization processes using the R-matrix method [23]. Our results demonstrated that the autoionizing resonance widths play an important role in determining the photoabsorption cross sections, and hence the radiative opacity.

Since DTA or DLA models can obtain accurate opacity for light elements, such detailed methods can be applied to temperature diagnostics. In many experimental investigations, Al is usually used to diagnose the temperature of the experimental sample.

However, for the radiative opacity of mid- and high-Z elements, there are unexplained systematic discrepancies between the theory and experiment so far (for example, see [24－26]). Perry *et al*. [24] experimentally measured the inner-shell X-ray absorption by a germanium plasma. Difference is evident between the experiment and STA theory. Later, Iglesias *et al*. [26] simulated the experimental spectra by using a DTA model. However, the discrepancy is still not

eliminated. Eidmann *et al*. [25] measured the opacity of a Au plasma at a density of ~ 0.01 g · cm^{-3} and temperature of ~ 20 eV in photon energy range of 50 to 300 eV. They also used the STA model to interpret the experimental spectra, yet the STA model predicted reversed intensity for the two strongest absorption peaks. Are the discrepancies for the opacity of mid- and high-*Z* elements caused by theoretical approximations or experimental uncertainties ?

In this paper, we review some typical opacity progresses by using the DTA and / or DLA methods, with the main emphasis on possible reasons for the theoretical and experimental discrepancies for mid- and high-*Z* plasmas. Theoretically, some physical effects that have been treated approximately or missed in theoretical models may affect the accuracy of opacity. For example, some discrepancies are supposed to be a consequence of line saturation effect [27], which can better be reproduced by a DLA model rather than statistical ones. DLA method usually predicts more accurate opacity than statistical ones, however, such a conclusion holds only if one takes main physical effects on the opacity into account. We will show that accurate opacity can be obtained by using the DLA method for mid- and high-*Z* plasmas, which are of great utility in many practical researches.

2 The formalism of the opacity model

The following processes contribute to opacities of plasmas:

(i) Bound-bound transitions,

$$A(\mathrm{i}) + h\nu \rightarrow A(\mathrm{f}) \tag{1}$$

(ii) Bound-free transitions,

$$A + h\nu \rightarrow A^{+} + e \tag{2}$$

(iii) Free-free transitions,

$$A + e_{\mathrm{i}} + h\nu \rightarrow A + e_{\mathrm{f}} \tag{3}$$

(iv) Scattering processes. The most important is electron scattering,

$$e_{\mathrm{i}} + h\nu \rightarrow e_{\mathrm{f}} + h\nu \tag{4}$$

in which there is a change in the directions of the photon but (at least for the case of Thomson scattering) no change in the photon frequency. At low temperatures, Rayleigh scattering can also contribute. In the above expressions, $h\nu$ refers to photon energy. Hence, the total opacity is given by:

$$\rho\kappa'(h\nu) = [\mu_{\mathrm{bb}}(h\nu) + \mu_{\mathrm{bf}}(h\nu) + \mu_{\mathrm{ff}}(h\nu)](1 - \mathrm{e}^{-h\nu/kT}) + \mu_{\mathrm{scatt}}(h\nu) \tag{5}$$

The prime on the opacity denotes that the stimulated emission has been taken into account.

Different theoretical methods take a different treatment on the above processes. For example, the UTA model [17, 18] assumes transition arrays as spectroscopical objects in their own right, characterized by their mean energy, spectral widths, and other properties. This approximation is good and useful if the array is unresolved. This model is connected with the statistics of lines and line strength and therefore is a statistical model. In the following, we only give detailed description of DLA and AA models, which are most relevant to the present work.

The bound-bound opacity for radiation of energy $h\nu$ can be obtained by summing the required bound-bound radiative transitions:

$$\mu_{bb}(h\nu) = \sum_{i}\left(\sum_{ll'} N_{il}\sigma_{ill'}(h\nu)\right) \tag{6}$$

where $\sigma_{ill'}(h\nu)$ is the cross section for photoexcitation from level l to l' and can be expressed in terms of the absorption oscillator strength $f_{ill'}$ as:

$$\sigma_{ill'}(h\nu) = \frac{\pi h e^2}{m_e c} f_{ill'} S(h\nu) = 109.71\, f_{ill'} S(h\nu) \tag{7}$$

where S is the line shape function with $h\nu$ in eV and $\sigma_{ill'}$ in Mb. If only the Stark broadening is considered, the line shape function has a Lorentzian profile. If only Doppler broadening is considered, the line shape function has a Gaussian profile. In general, the observed spectral profile is neither simply Gaussian nor Lorentzian, but a convolution of the two profiles, i.e., the Voigt profile

$$S(h\nu) = \frac{\sqrt{\ln 2}}{\sqrt{\pi}\Gamma_d} H(a, v) \tag{8}$$

where $H(a, v)$ is the Voigt function:

$$H(a,v) = \frac{a}{\pi}\int_{-\infty}^{+\infty} \frac{\mathrm{e}^{-x^2}}{a^2 + (v-x)^2}\,\mathrm{d}x$$

$$a = \sqrt{\ln 2}\,\Gamma_l / \Gamma_d$$

$$v = \sqrt{\ln 2}\,(h\nu - h\nu_0)/\Gamma_d$$

where Γ_d and Γ_l are the Doppler and Stark half width at half maximum (HWHM), respectively. The Doppler HWHM is related to the temperature T of the plasma and transition energy $h\nu_0$ [30]:

$$\Gamma_d = 3.858\times10^{-5}(kT/A)^{1/2}(h\nu_0) \tag{9}$$

where A is atomic weight of the ion in gram and the units of kT, $h\nu_0$ and Γ are eV. The Stark HWHM (in eV) can be obtained by semiempirical method [28, 29]:

$$\Gamma_l = N_e \frac{8\pi}{6}\frac{\hbar^3}{m^2 e}\left(\frac{2m}{\pi \mathrm{k}T}\right)^{1/2}\frac{\pi}{\sqrt{3}}\left(0.9 - \frac{1.1}{z}\right) \cdot \sum_{j=\mathrm{i},\mathrm{f}}\left(\frac{3n_j}{2z}\right)^2 (n^2 - l_j^2 - l_j - 1) \tag{10}$$

where n_{i} (l_{i}) and n_{f} (l_{f}) are the effective principal (the orbital angular momentum) quantum numbers of the lower and upper energy levels of the transition, respectively. Other such type of broadening mechanisms, such as autoionization resonance broadening, should also be included in the expression of Γ_l.

The contribution of bound-free absorption can be ob-

tained from the photoionization cross sections per ion:

$$\mu_{\mathrm{bf}}(h\nu)=\sum_i N_i\sigma_i(h\nu) \tag{11}$$

where $\sigma_i(h\nu)$ is the photoionization cross section per ion i and it can be calculated from the photoionization cross sections $\sigma_{il}(h\nu)$ from term l in ion I:

$$\sigma_i(h\nu)=\sum_l \frac{g_{il}\mathrm{e}^{-E_{il}/kT}}{Z_i}\sigma_{il}(h\nu) \tag{12}$$

where Z_i is the partition function for ion i, which will be defined later.

The free-free opacity is given by:

$$\mu_{\mathrm{ff}}(h\nu)=\sum_i N_i\sigma_{\mathrm{ff}}(h\nu) \tag{13}$$

where $\sigma_{\mathrm{ff}}(h\nu)$ is the Kramers cross section:

$$\sigma_{\mathrm{ff}}(h\nu)=\frac{16\pi^2e^2h^2}{3\sqrt{3}c(2\pi m)^{3/2}}\frac{z^3N_ig_{\mathrm{ff}}}{(kT)^{1/2}(h\nu)^3} \tag{14}$$

where z is the ionic charge, the free-free Gaunt factor, g_{ff}, is taken as unity. The scattering contribution to the opacity μ_{scatt} is approximated using Thomson scattering cross section.

To obtain the opacity, one needs to know the populations of relevant levels for different ionization stages. If the density of plasmas is high enough, then the plasmas will be in LTE. If the density is low, the plasmas will be in coronal equilibrium. Otherwise, the plasmas will be between the two equilibriums. For an LTE plasma, the population distributions of different ionization stages are given by Saha equation [30]:

$$\frac{N_{i+1}N_e}{N_i}=\frac{Z_eZ_{i+1}}{Z_i}\mathrm{e}^{-\frac{\phi_i-\Delta\phi_i}{kT}} \tag{15}$$

where N_i is the total population density of ion i, N_e is the number of free electrons per unit volume, ϕ_i is the ionization potential of ion i, $\Delta\phi_i$ is the depression of ionization limit caused by plasma environment restricting the number of bound states available, Z_i and Z_e are the partition functions for ion i and free electron, respectively. Z_i is given by:

$$Z_i=\sum_l g_{il}\mathrm{e}^{-E_{il}/kT} \tag{16}$$

and Z_e by

$$Z_e=2\left(\frac{2\pi m_ekT}{h^2}\right)^{3/2} \tag{17}$$

where $g_{il}=2(J+1)$ is the statistical weight, E_{il} is the energy of level l of ion i above the ground state, k is the Boltzmann constant, T is the temperature, m_e is the electron mass and h is the Planck constant. The upper limit to the sum (16) is given by the same ionization depression as for the Saha equation. The population density N_{il} for level l of ion stage i is given by the Boltzmann distribution function:

$$N_{il}=g_{il}(N_i/Z_i)\mathrm{e}^{-E_{il}/kT} \tag{18}$$

The Saha equation is solved with the constraint of particle and charge conservation.

In solving the Saha equation, a calculation of the ionization potential depression (IPD) is needed to give a finite limit to the partition functions. There are a number of methods by which the IPD can be calculated (for example, see [31]), such as the Debye-Huckel model, Stewart-Pyatt approximation and the ion-sphere model. It is well known that the use of the IPD in this manner leads to discontinuous derivatives of the free energy, but it is not important for interpreting experimental results. As the influence on the transmission spectrum due to the three different models is small, we choose the first one. For the Debye-Huckel model of the plasma potential, the largest radius of an electron that can still be bound is given by the Debye radius. As the principle quantum number becomes larger, the ions behave more and more hydrogenic. In this case the IPD is given by:

$$\Delta\phi_i=\frac{ze^2}{4\pi\varepsilon_0}\sqrt{\frac{e^2N_e}{\varepsilon_0kT}} \tag{19}$$

where z is the charge of the species of interest ($z=1$ for neutral).

In practical applications, such as energy transfer through hot dense matter, Rosseland and Planck mean opacities are required. These two mean opacities are defined by:

$$\frac{1}{K_{\mathrm{R}}}=\int_0^\infty\frac{W_{\mathrm{R}}(u)\mathrm{d}u}{\kappa'(u)} \tag{20}$$

and

$$K_{\mathrm{P}}=\int_0^\infty(\kappa'(u)-\kappa_{\mathrm{scatt}}(u))\,W_{\mathrm{P}}(u)\mathrm{d}u \tag{21}$$

where $u=h\nu/kT$, $\kappa_{\mathrm{scatt}}(u)$ is the opacity contributed by scattering, W_{R} and W_{P} are Rosseland and Planck weighting functions, respectively, given by:

$$W_{\mathrm{R}}(u)=\frac{15}{4\pi^4}\frac{u^4\mathrm{e}^{-u}}{[1-\mathrm{e}^{-u}]^2}$$

and

$$W_{\mathrm{P}}(u)=\frac{15}{\pi^4}\frac{u^3\mathrm{e}^{-u}}{1-\mathrm{e}^{-u}}$$

In experimental investigations, transmission is measured to obtain the opacity. The fraction of radiation transmitted F at energy $h\nu$ with respect to some incident source of arbitrary intensity is given by:

$$F(h\nu)=\mathrm{e}^{-\mu(h\nu)L} \tag{22}$$

where L is the path length traversed by the light source through the plasma. In order to compare with the experiment, the theoretical transmission is integrated over a Gaussian function, with the FWHM corresponding to the spectrometer resolution transmission spectrum.

In the above, detailed description has been given on the theoretical method of DLA formalism. In some cases, we compared the DTA or DLA results with those of the AA model [32, 33].

3 Typical results and discussions

In this section, we present some typical results for the opacities of low-, mid- and high-Z plasmas. For low-Z plasmas, we take Al as an example. For mid-Z plasmas, we consider Fe and Br elements. Au plasma is typical high-Z material, which is widely used in many practical research fields such as ICF.

3.1 Radiative opacity of Al plasmas

3.1.1 X-ray transmission of Al *plasmas*

Under the prototype experiment carried out by Davidson *et al.* [6], the FWHM of Doppler broadening is approximately 0.14 eV for an aluminum plasma at $kT = 40$ eV and a photon energy of 1500 eV. The effect of electron collision broadening was estimated [34] to be a factor of 5 less than the Doppler width for the plasma conditions and the photon energy range of interest. Most theoretical work had taken Doppler broadening into account. However, our research [22] showed that the autoionizing width is usually larger than the Doppler width and becomes the major broadening mechanism.

The effect of autoionizing resonance broadening on the transmission can be seen clearly from Fig. 1, where the calculated transmission has been convolved with the spectrometer resolution 0.7 eV, which is the same with that used by Abdallah and Clark [20]. To simulate the experiment, the path length L is chosen to be 0.004 cm. The results presented in Fig. 1 are obtained by assuming two different line profiles, Voigt and Gaussian. The width of the Voigt profile was determined by a convolution of a Lorentzian profile and a Gaussian profile. The width of the Lorentzian profile is taken approximately to be the autoionizing width and the width of the Gaussian profile is taken to be the Doppler width. The solid line refers to the final transmission spectrum obtained by using the Voigt profile, the dashed one to the transmission spectrum by Gaussian profile, and the dotted one to the experimentally observed spectrum. Therefore, the result of solid line has included the Doppler and autoionizing broadening. The labels at the top of the Figure indicate the dominant i charge states of aluminum in each energy region.

It can be seen from Fig. 1 that the agreement between the calculated spectrum using the Voigt profile (*solid lines*) and the experimental spectrum is good both for the spectral intensity and position, but a large difference exists by using the Gaussian profile, especially for the lower ionization stages such as Al^{5+}, Al^{6+} and Al^{7+}. This is because these ions have relatively large autoionizing resonance widths. According to our calculation, the typical autoionizing resonance widths are approximately 0.29, 0.24, 0.20, 0.11, and 0.08 eV from Al^{5+} to Al^{9+}, respectively. From the comparison of the two calculated spectra with the experimental result, one can conclude that the theoretical calculations with only taking account of the Doppler broadening would result in a too slow convergence to the observed spectra. For the K-shell transitions from the low-lying states, autoionizing resonance broadening, an actually existing physical effect, is the major broadening mechanism and should be taken into account in calculating the spectral resolved transmission.

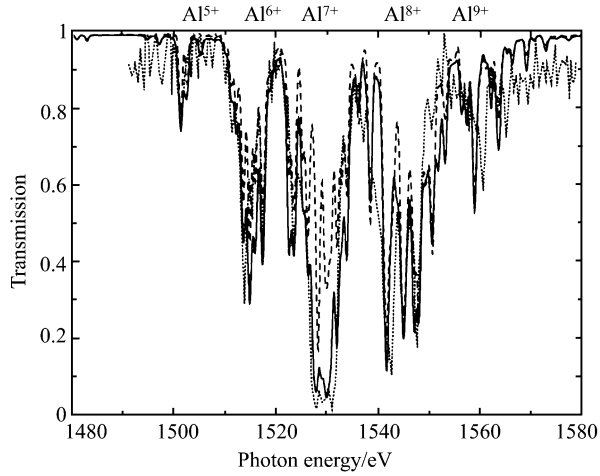

Fig. 1 Transmission calculated as a function of photon energy in eV by using CIV3 code with the instrumental broadening have been considered. The temperature and density are 40 eV and 0.0135 g · cm^{-3}, respectively. The solid and dashed lines refer to the theoretical results with Voigt and Gaussian line shape functions, respectively. The dotted line refers to the experimental spectrum. The labels at the top of the Figure indicate the dominant ion charge states of aluminum in each energy region.

The lines in the X-ray energy region are contributed by the 1s—2p transitions. The upper states are inner-shell autoionized excited ones, thus a better choice should be treating the 1s—2p transitions as photoionization processes, which are naturally fulfilled by the R-matrix method [23]. The transmission spectrum obtained by using the R-matrix photoabsorption cross sections is given in Fig. 2. Figure 2 (a) shows the transmission that does not include instrumental broadening. This spectrum is highly resolved and shows that many 1s—2p lines are contributing to the transmission. Figure 2 (b) shows a solid line derived by convolving the curve shown in Fig. 2 (a) with spectrometer resolution. The dotted line shows the experimental spectrum. The calculated spectrum is in satisfactorily good agreement with the experiment. Not only are all the major structures present, but also the intensities agree well. Except for the Al^{7+}, the positions of the spectrum of other ionization stages have a little shift compared to the experimental spectrum. Al^{8+} and Al^{9+} shift toward the lower photon energy, while Al^{5+} and Al^{6+} shift a little toward the higher photon energy. This may be due to the fact that different ions have different electrons and thus different correlation energies. For comparison, we also give the theoretical spectrum of Abdallah and Clark [20] shown as a dashed line. They obtained the results by carrying out a much larger-sized calculation than ours. In their treatment, oscillator strengths were computed for all possible bound-bound transitions among all possible excited electron orbitals with $n < 11$ and $l < 5$.

Good agreement was also obtained by Iglesias *et al*. [21] with a limit of $n < 8$ and $l < n$. What we can conclude is that their calculations converge with the electron orbitals slower than the present case due to the neglect of the autoionization resonance broadening.

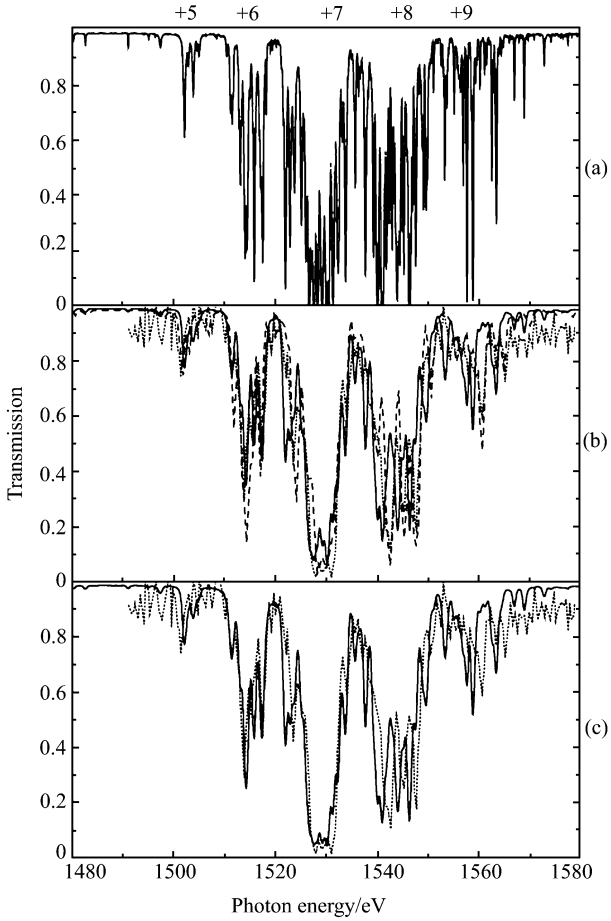

Fig. 2 Transmission calculated as a function of photon energy in eV by using R-matrix method. The temperature and density are 40 eV and 0.0135 g · cm^{-3}, respectively. In **(a)**, the solid and dashed lines refer to the length and velocity forms by using the Voigt profile. The agreement between the two forms are so good that they cannot be distinguished. In **(b)**, the solid line are obtained by integrating curve **(a)** using the reported spectrometer resolution, and the dashed one is the result of Abdallah and Clark [20]. In **(c)**, the solid line refers to the result obtained by combining the *R*-matrix and CIV3 CI method to include more satellite lines. In **(b)** and **(c)**, the dotted line refers to the experimental spectrum carried out by Davidson *et al*.

In order to make the *R*-matrix calculations manageable, we only include orbitals up to $n = 3$. The contributions of some satellite lines from highly excited states are not included in the calculations. In order to access the convergence of the present *R*-matrix calculation, we have included more satellite lines by using the CIV3 code. In this calculation, in addition to the transitions treated by the *R*-matrix scheme, we have considered more satellite lines with the initial states above the highest term treated by the *R*-matrix method. These additional satellite lines are restricted to the excited states of having one electron in the orbitals of $3 \leqslant n' \leqslant 8$ and $l' \leqslant 4$. Because the autoionizing width of these satellite lines are much smaller than the Doppler width, their inclusion by using the CIV3 code does not reduce the generality of this method. The result is shown in Fig. 2 (c). It can be easily seen that our R-matrix calculation is basically converged. The inclusion of the contributions of more satellite lines can improve the final spectrum slightly.

Next, let us turn to the experiment done by Perry *et al*. [8]. In this experiment, the main ionization stages ranged from AlVIII through AlXII and the typical Doppler FWHM of 1s to 2p transitions is approximately 0.18 eV. Because of different experimental conditions, higher ionization stages had been created than in the experiment by Davidson *et al*. As have been shown above, the autoionizing resonance widths of the K-shell excited states of the ions present in the experiment of Perry *et al*. [8] are less than the Doppler broadening and the Doppler broadening becomes the main broadening mechanism. For this case, the inclusion of the autoionizing resonance broadening will not change the convergence behavior as much as in the above calculation, and the relativistic effect may have large influence on the transmission spectrum. Figure 3 shows the results obtained by multi-configuration Hartree-Fock (MCHF) [35] calculations with both the LS nonrelativistic and the Breit-Pauli LSJ relativistic formalisms. The solid line refers to the relativistic calculation and the dashed one to the nonrelativistic result. The dotted line refer to experimental spectrum. In performing the MCHF calculation, the maximum principal and angular momentum quantum numbers of the orbitals are considered up to $n' = 8$ and $l' = 5$ (h orbitals). One can easily see that rather good agreement is obtained between the calculated and experimental spectra after taking account of the relativistic splitting.

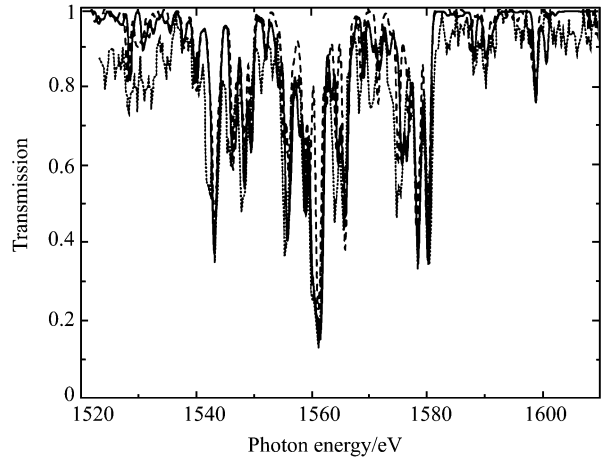

Fig. 3 Transmission calculated as a function of photon energy in eV under the experimental condition of Perry *et al*. [8] with temperature T = 58 eV and density ρ = 0.02 g · cm^{-3} by using MCHF LS nonrelativistic (*dashed line*) and LSJ relativistic formalism (*solid line*) compared with the experiment (*dotted line*).

3.1.2 Opacity and transmission at 20 eV *and* 0.01 g · cm^{-3}

We [33] have calculated the radiative opacity under the experimental condition of Winhart *et al*. [13, 14] with the

temperature of 20 eV and density of 0.01 g · cm^{-3}. In their experiment, the aluminum sample layer was 107.5 nm ($\rho L = 30$ μg · cm^{-2}) and thus the path length L was deter mined to be 0.003 cm. The time resolution was 20 ps and the wavelength resolution 0.1 nm.

Figure 4 shows the opacity contributed by bound-bound absorption. It can easily be seen that the bound-bound absorption consists of two main distinct structures. The 0—70 eV energy range consists of 2s—2p transitions and 70—215 eV energy range the 2p—*n*s and 2p—*n*d transitions. For examples, the three strongest lines located at 41, 46 and 52 eV are attributed to the 2s—2p bound-bound transitions from Al V and Al VI ions. The prominent line absorptions near 77, 97 and 116 eV are from the 2p—3s transitions contributed by Al IV, Al V and Al VI ions, respectively. As we will demonstrate later, these 2p—3s absorption lines constitute the most striking structures in the experimental transmission spectrum The absorptions near 140 and 165 eV are caused by the 2p—3d transitions of Al V and Al VI ions. Above 240 eV, there are no true bound-bound transitions. The widths of the lines are large enough to fill the gaps between the discrete spectral lines. In the photon energy range shown in the plot, the Stark width is much more larger than the Doppler width, thus the Stark broadening is the major broadening mechanism. As we have demonstrated in a recent paper [37], the Planck mean opacities are nearly equal with and without considering the Stark width, but the Rosseland mean opacities differ consid erably depending on whether or not the Stark broadening is taken into account. The Rosseland mean opacities are sensitive to the detailed profile and corresponding width.

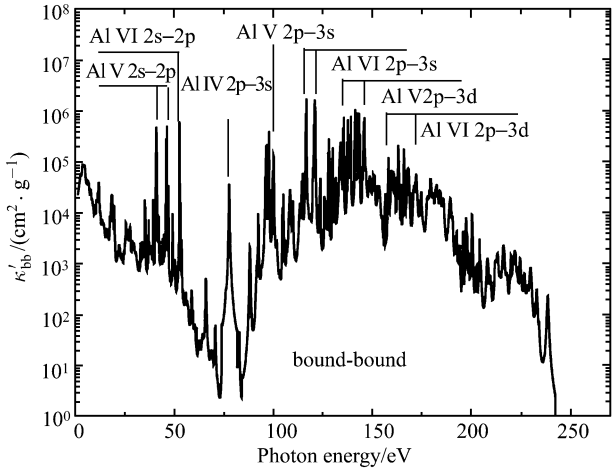

Fig. 4 The radiative opacity contributed by bound-bound absorption for Al plasma at a temperature of 20 eV and a density of 0.01 g · cm^{-3}.

Figure 5 shows the opacity contributed by the bound-free absorption, with Fig. 5 (a) referring to the result of only taking account of autoionization resonance width and Fig. 5 (b) to the result of including both the autoionization resonance width and the Stark width. The opacity shown in Fig. 5 (a) is obtained directly from our *R*-matrix photoionization cross sections. From the inspection of Fig. 5 (a), one can see that the autoionization resonance width is not large enough to fill the gaps between the resonances. In fact, under the experimental condition considered, the Stark full width is the largest among all the broadening mechanisms and therefore becomes the major factor to be considered. In order to take account of the Stark broadening, we convolute the curve shown in Fig. 5 (a) with a Lorentzian profile function, with the full width corresponding to the Stark width. From the estimation of the Stark full width, we take it to be 0.4 eV. The final result after the Stark broadening has been included is shown in Fig. 5 (b). In this case, the resonance structures coalesces to fill the gaps between them. Many resonance structures are greatly smoothed and some smaller ones can no longer be seen after the convolution. The values of the resonances in the opacity spectrum have also been greatly reduced. The maximum opacity in Fig. 5 (a) is more than 2× 10^6 cm^2 · g^{-1}, whereas in Fig. 5 (b) less than 4×10^5 cm^2 · g^{-1}. These results show that the autoionization widths of the valence-shell excited states are in generally by far smaller than the Stark widths.

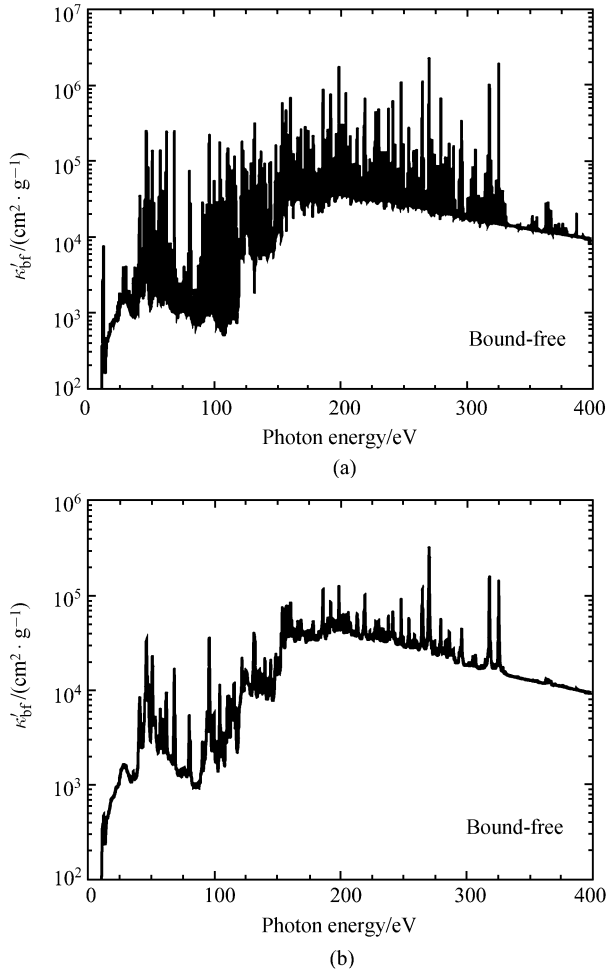

Fig. 5 The radiative opacity contributed by bound-free absorption for Al plasma at a temperature of 20 eV and a density of 0.01 g · cm^{-3}: **(a)** with only the autoionization resonance width being taken account of and **(b)** with both the autoionization resonance width and Stark width (0.4 eV) being considered.

Figure 6 shows a solid line representing the total opacity with the bound-free absorption shown in Fig. 5 (b). One can see that below 200 eV, the major absorption structures in the total opacity are caused by bound-bound transitions; above 200 eV, the structures are mainly caused by the autoionization resonances. It seems that some of these autoionization resonances were not fully included in the opacity models [38—42] mentioned above. This can be illustrated later by comparing the theoretical transmission obtained by OPAL [38] with the experimental one. The Rosseland and Planck mean opacities obtained according to Eqs. (20) and (21) are 4184 and 24 891 $cm^2 \cdot g^{-1}$, respectively. In order to have a comparison with the opacity obtained by the average atom (AA) model, we have also carried out calculations using the AA model. The result is shown in Fig. 6 with a dashed line. One can see that all the structures are smoothed into a few broad peaks in the AA model. The opacities for the DTA and AA models above 220 eV are nearly equal except for those at the energies of the resonance structures. Below 220 eV, however, a large difference exists between the two models. The opacity obtained by the AA model is considerably larger than that by the DTA model for photon energy from 20 eV to 120 eV. This difference will, of course, cause a large difference between the two models for the Rosseland and Planck mean opacities not only because the opacities obtained from the two models differ considerably, but also because the maxima of the Rosseland and Planck weighting functions are located in this photon energy range (The Rosseland and Planck weighting functions reach their maxima at approximate 77.6 and 56.8 eV, respectively, at the temperature of 20 eV). The Rosseland and Planck mean opacities are 22 520 and 30 402 $cm^2 \cdot g^{-1}$, respectively, for the AA model. The Rosseland mean opacity by the AA model is more than 4 times larger than that by the DTA model. The Planck mean opacity, on the other hand, does not have such large difference between the two models. The value obtained by the AA model is larger than that by the DTA model by only 22 %.

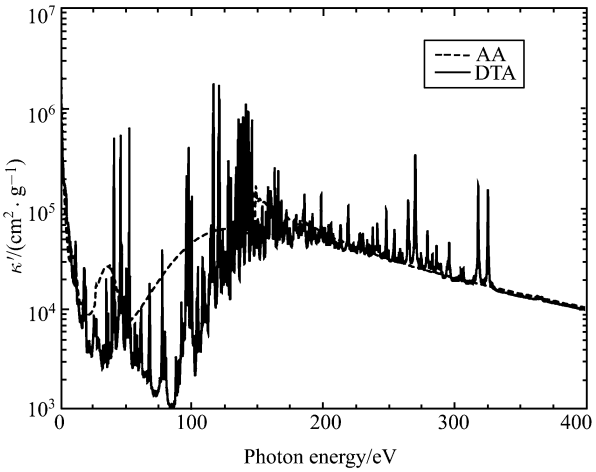

Fig. 6 The total radiative opacity for Al plasma at a temperature of 20 eV and a density of 0.01 $g \cdot cm^{-3}$: the solid line refers to the DTA calculation and the dashed line to the AA model. For DTA model, $K_R = 4184\ cm^2 \cdot g^{-1}$, $K_P = 24\,891\ cm^2 \cdot g^{-1}$; For AA model, $K_R = 22\,520\ cm^2 \cdot g^{-1}$, $K_P = 30\,402\ cm^2 \cdot g^{-1}$.

In order to testify the correctness and accuracy of our calculations, we have derived the transmission from the calculated opacity shown in Fig. 6 to compare with the experimental spectrum. Figure 7 (a) shows the transmission in the energy range from 70 eV to 250 eV, which corresponds to the range measured by the experiments [13, 14]. In this plot, the instrumental broadening has not been included. Figure 7 (b) shows a solid line obtained by convoluting the curve shown in Fig. 7 (a) with the spectrometer resolution, which varies with the photon energy. The dashed line in Fig. 7 (b) refers to the experimental spectrum. From the comparisons of Figs. 7 (a) and 7 (b), one can easily see that the spectrum shown in Fig. 7 (a) is more highly resolved than that in Fig. 7 (b). The detailed features shown in Fig. 7 (a) should be observable in high-resolution measurements. Generally good agreement is found between our DTA result and the experiment. In Figs. 7 (a) and 7 (b), the most striking structures near 75, 95 and 114 eV are caused by the 2p—3s bound-bound transitions of Al IV, Al V and Al VI ions, respectively. The structures around 140 eV and 165 eV are caused by the 2p—3d transitions of Al V and Al VI ions, respectively. The structures caused by 2p—3d transitions are

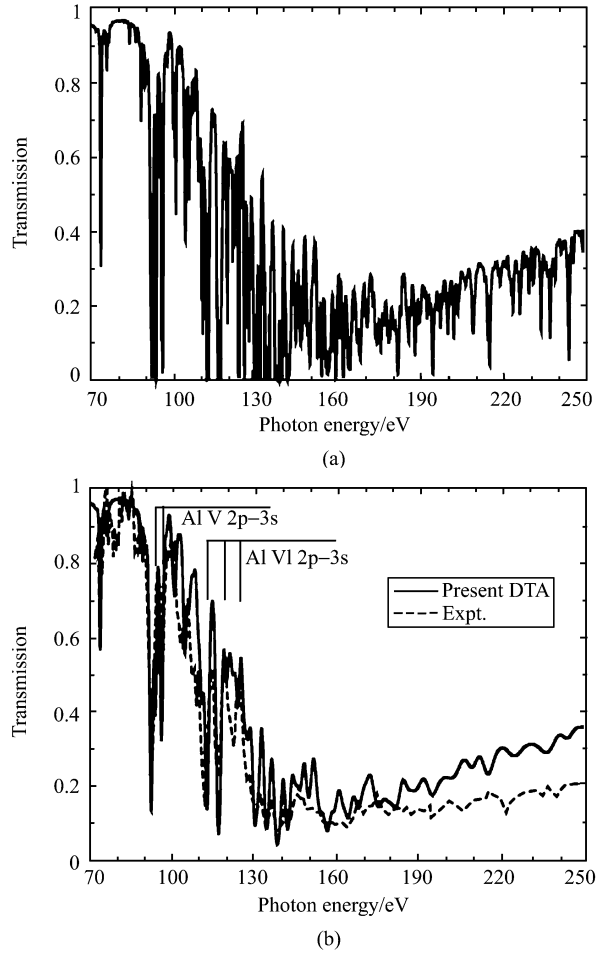

Fig. 7 Transmission calculated as a function of photon energy in eV using DTA approximation: **(a)** The instrumental broadening having not been considered and **(b)** integrating curve **(a)** using the reported spectrometer resolution (*solid lines*). Note that the spectrometer resolution are varied with photon energies. The dashed line is the experimentally observed spectrum [13].

made less striking by the stronger bound-free background absorption. In fact, the 2p－3d lines are stronger than those of 2p－3s ones. At higher photon energies (above 160 eV), however, many structures shown in 7 (a) are greatly smoothed after taking account of the instrumental effects. The big differences shown in Figs. 7 (a) and 7 (b) (the solid line) are, undoubtedly, caused by the instrumental broadening. As reported in the experiment [13, 14], the wavelength resolution was 0.1 nm. According to this wavelength resolution, the energy resolution varies considerably in the energy range from 70 eV to 250 eV, since the energy resolution is in proportion to the square of the photon energy. For example, the energy resolution is 0.82 eV at 100 eV, while it is increased to 1.84, 3.2 and 5.1 eV at 150, 200 and 250 eV, respectively. Because of the low energy resolution at the higher photon energies in the experiment, the structures are smoothed more greatly near the higher energy edge.

One of the most accurate opacity models among those mentioned above is the OPAL [38]. It obtained better agreement with the experiment [13, 14] than did other models [39－42], therefore, we only compare our DTA transmission spectrum with that of the OPAL [38]. The result is shown in Fig. 8 (a), with the solid line referring to our DTA transmission, the long dashed line to the transmission obtained by the OPAL and the dashed line to the experimental spectrum. One can see that at lower photon energies (less than about 150 eV), both theoretical calculations exhibit similar structures to the experiment. At these lower photon energies, the autoionization resonances do not have large effects on the opacity or transmission. This is because the opacities caused by the autoionization resonances are by far smaller than those by bound-bound absorption. This conclusion can easily be seen from the comparison of the opacities contributed by the bound-bound and bound-free absorptions, which are shown in Fig. 4 and Fig. 5 (b). The maximal opacity caused by bound-bound absorption is more than 10^6 cm$^2\cdot$g^{-1}, while that by bound-free is about 4×10^4 cm$^2\cdot$ g^{-1}. Moreover, the back- ground of the bound-free absorption is relatively large because this photon energy range is very close to the ionization threshold.

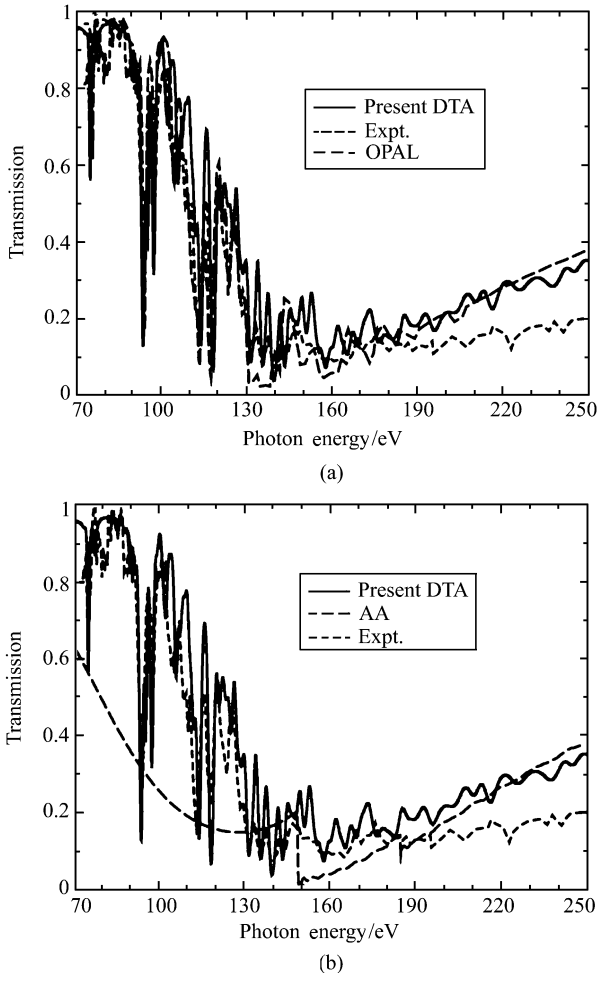

Fig. 8 Comparisons between our DTA simulation and other theoretical models: **(a)** OPAL [35] and **(b)** AA.

At the higher photon energies, however, our DTA transmission exhibits more structures than that of the OPAL [38]. OPAL [38] did not reproduce some structures at the higher photon energies, while these structures are indeed verified in the experiment [13, 14]. We attribute the structures at the higher photon energies to the more detailed treatment of the photoionization process in our calculations. However, both two models deviate from the experimental spectrum at the higher photon energies. The deviation becomes larger and larger as the photon energy becomes higher and higher until it reaches 250 eV. The deviation of both models from the experiment may be caused by the noise, but, generally, the noise cannot cause the structures. In order to demonstrate the existence of the structures at the higher photon energy range, we have traced out their origins. We maintain that the structures observed by the experiment [13, 14] at the higher photon energies should be real, not just noise.

The transmission obtained by the AA model is also compared with our DTA and the experimental spectra, which is shown in Fig. 8 (b). At lower energies, the transmission obtained by the AA model differs greatly from that of the DTA and of the experiment. Near the higher energy edge, on the other hand, the transmission obtained by the AA and DTA models are nearly equal in average, except that the AA model cannot reproduce the resonance structures above the threshold.

3.1.3 *Opacities of the* 40 eV *isothermal sequence*

The differences between the spectrally resolved and mean opacities under the above typical experimental condition [13, 14] obtained by the DTA and AA models are due to two main sources. The first one is the energy shift of the absorption peaks of the AA model relative to the true positions. The second one is the smoothness of the fine line structures made artificially in the AA model. As defined in the theoretical method, the Planck mean opacity is a linear weighted average, while the Rosseland mean opacity is a harmonic weighted average. Therefore, the nonphysical energy shift of the absorption peaks of the AA model induces errors in both

the Rosseland and Planck means, while the smoothness over the detailed lines in the AA model changes mainly the Rosseland mean opacity. The question is when both of, one of, or even none of these two factors are significant to cause unacceptable errors. To have an overall view on the question, we [37] have made a systematic study on the spectrally resolved and Rosseland and Planck mean opacities under different plasma conditions for three sequences: a 40 eV isothermal one, a 0.01 $g \cdot cm^{-3}$ isodense one and an average ionization degree $Z^* \sim 7.13$ one. In this part, we discuss the first one.

Figures 9 (a)—(d) show the spectrally resolved radiative opacities at the density of 0.0001, 0.001, 0.01 and 0.1 $g \cdot cm^{-3}$, respectively. The solid lines refer to the DTA opacities and the grey lines to the AA opacities. One can see from Figs. 9 (a)—(b) that at the densities of 0.0001 and 0.001 $g \cdot cm^{-3}$, the widths of the spectral lines are too small to coalesce to fill in the gaps between the discrete lines. As a matter of fact, the Stark and Doppler widths are indeed small and they compete with each other for different transitions for plasmas at the density of 0.001 $g \cdot cm^{-3}$.

To have a quantitative understanding, we turn to the line widths caused by the two kinds of broadening mechanisms. For aluminum plasma at a temperature of 40 eV and a density of 0.001 $g \cdot cm^{-3}$, Al X ions are the most abundant, representing 42 % of the total particle population, according to our calculation. For a transition of 2p—3d from the ground state of Al X, the Stark width can be calculated to be 2 meV from Eq. (4) and the Doppler width is 10 meV. The Doppler width is 4 times larger than Stark width. While for a transition of 2s—2p from the ground state of Al X, the Stark width is 1 meV and the Doppler width is 0.8 meV. In this case, the Doppler width is a little smaller than the Stark width. One can imagine that the Doppler broadening will dominate gradually as the density of the plasma decreases. When the density is decreased by 10 times, i.e., 0.0001 $g \cdot cm^{-3}$, the Doppler broadening is the main broadening mechanism. On the other hand, when the density is increased by 10 times, i.e., 0.01 $g \cdot cm^{-3}$, the Doppler widths are basically the same as those of 0.001 $g \cdot cm^{-3}$ density, but the Stark widths have been increased greatly because the electron density has been increased considerably. From the inspection of Fig. 9 (c), one can see that although there are still non-overlapping between some lines, some other lines begin to coalesce to fill the gaps. When the density is increased further to 0.1 $g \cdot cm^{-3}$, the Stark width becomes so large that all the absorption lines overlap greatly. They have merged into a much more smoother curve. At this density, the Stark broadening dominates over Doppler broadening. The spectrally resolved opacities obtained by our DTA model becomes more and more closer to those obtained by AA model with the increase of the density. From these analyses, one can conclude that the differences between the Rosseland mean opacities obtained by the two models become larger and larger as the mass densities get lower and lower. On the contrary, with the increase of the density, the agreements between the Rosseland and Planck mean opacities by the two models will become closer and closer. The final results are indeed so and such a conclusion can easily be seen from Fig. 10, which shows the variations of the Rosseland and Planck mean opacities as a function of the density.

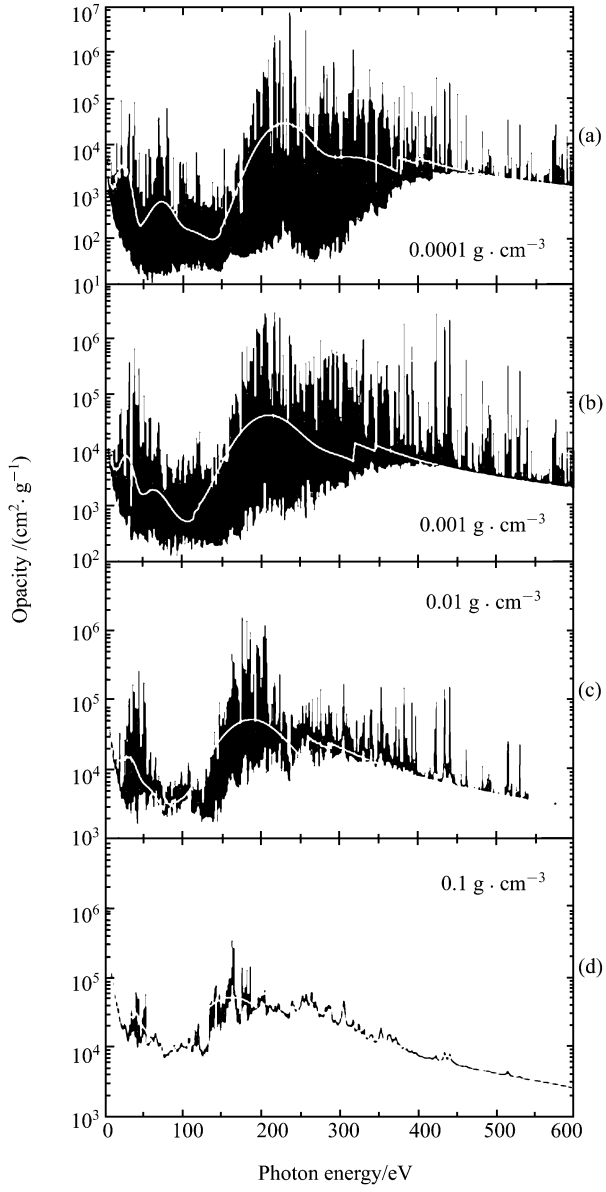

Fig. 9 The spectrally resolved radiative opacities for aluminum plasmas at a temperature of 40 eV and densities of: **(a)** 0.0001, **(b)** 0.001, **(c)** 0.01 $g \cdot cm^{-3}$ and **(d)** 0.1 $g \cdot cm^{-3}$. The solid lines refer to the DTA results and the grey lines to the AA results.

From the inspection of Fig. 10, one can see that the agreements between the Planck mean opacities obtained by the DTA and AA models are better than those of the Rosseland mean opacities. The relative difference between the DTA and AA Planck mean opacities is less than 14 %. It is 13.6 %

at the density of 0.0001 g · cm^{-3} and decreases to 1.5 %, 3.6 % and 0.34 % at the densities of 0.001, 0.01 and 0.1 g · cm^{-3}, respectively. From Fig. 10, one can see that the agreements between the Rosseland mean opacities obtained by our DTA and AA models become better and better as the density increases. For the densities above 0.01 g · cm^{-3}, the differ ence between the DTA and AA Rosseland mean opacities is no more than 40 percent. This conclusion is also temperature dependent. Both the Rosseland and Planck mean opacities increase monotonically with density over the 0.0001—0.64 g · cm^{-3} range, for either DTA or AA models.

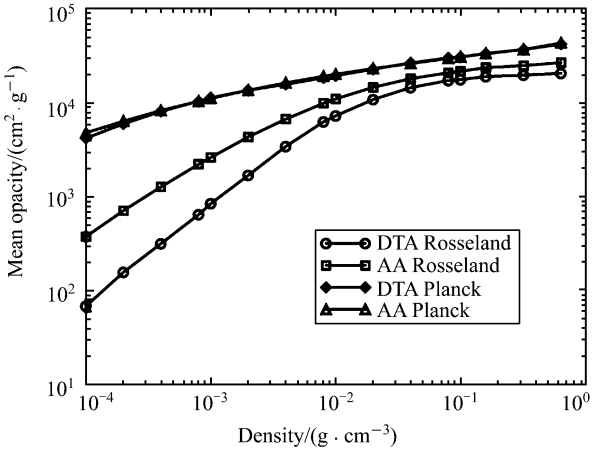

Fig. 10 The Rosseland and Planck mean opacities for aluminum plasmas as a function of density at a temperature of 40 eV.

3.1.4 Opacities of the 0.01 g · cm^{-3} *isodense sequence*

Below, we turn to the opacities at a density of 0.01 g · cm^{-3} and temperatures from 15 to 60 eV. Figures 11(a)—(d) show the spectrally resolved opacities at a temperature of 20, 30, 50, and 60 eV, respectively. From the inspection of Fig. 11, one can find that the spectral line shapes and widths do not differ considerably at different temperatures, but the maximal value of the opacities shifts toward a higher photon energy as the temperature increases. The latter conclusion can be easily understood because the average ionization degree of the plasma increases as the plasma temperature increases. The increase of the average ionization degree means that the most abundant ions in the plasma shift to the higher ionization stage. For the same type of transitions from different ionization stages, for example, 2p—3s, the transition energies of the higher ionization stages are usually larger than those of lower ionization stages. Therefore, the maximal value of the opacities shifts toward higher photon energy as the temperature increases. The former conclusion cannot be seen as directly as the latter one. The semiempirical expression of the Stark width shows that the Stark width increases with electron density, while it decreases with ionic charge. With the increase of temperature and density unchanged, the average ionization degree will increase. As a result, the electron density and ionic charge of the most populated species will increase with higher temperature. The competition between the two factors results in the closeness of the line widths for isodense sequence. The positions of the main absorption peaks around 200 eV predicted by the DTA and AA models coincide generally well at the temperatures above 30 eV. As expected, the Planck mean opacities of the two models for these temperatures do not differ quite much.

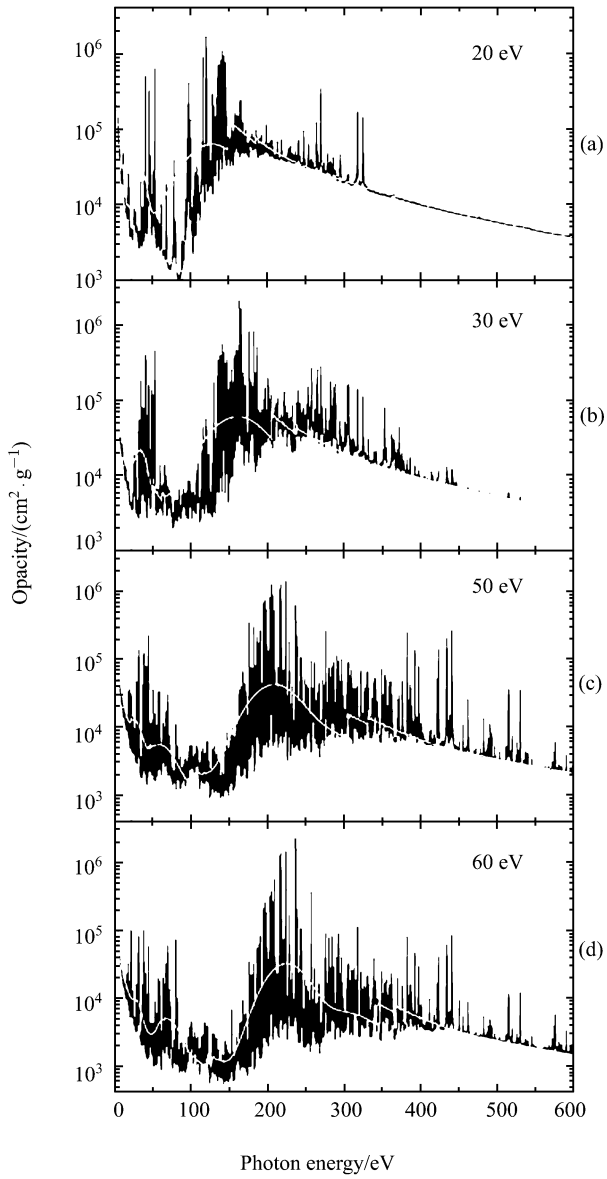

Fig. 11 The spectrally resolved radiative opacities for aluminum plasmas at a density of 0.01 g · cm^{-3} and temperatures of: **(a)** 20 eV, **(b)** 30 eV, **(c)** 50 eV and **(d)** 60 eV.

Figure 12 shows the variations of the two means with the temperature. From Fig. 12, one can see that the variation of the two mean opacities with the temperature is more complicated than with the density. The Planck mean opacities obtained by our DTA and AA models have larger differences

at temperatures below 30 eV (the maximum of which is 23.6 % at 22 eV) than at temperatures above 30 eV (the maximum is 8.7 % at 55 eV). Both our DTA and AA models show a shoulder at the temperature of about 25 eV. At about 45 eV, the Planck mean opacities from the DTA and AA models are equal to each other. For the Rosseland mean opacities, both models predict a similar trend in the temperature range of 15—60 eV. They increase with temperature at first and then decrease, but the temperature of the turning point is different. The DTA model predicts a maximum Rosseland mean at about 35 eV, while the corresponding AA at about 20 eV. The difference of the Rosseland mean between the two models is caused by the different treatment of the bound-bound and bound-free absorption processes. At the temperature of 20 eV, the AA Rosseland mean is 4.38 times larger than the corresponding DTA value. With the increase of temperature, the differences begin to decrease. At the temperature of 35 eV, the AA Rosseland mean is only 66 % larger than the corresponding DTA value. At above 35 eV, the differences become even smaller. At 60 eV, the relative difference between the two models is only 29 %.

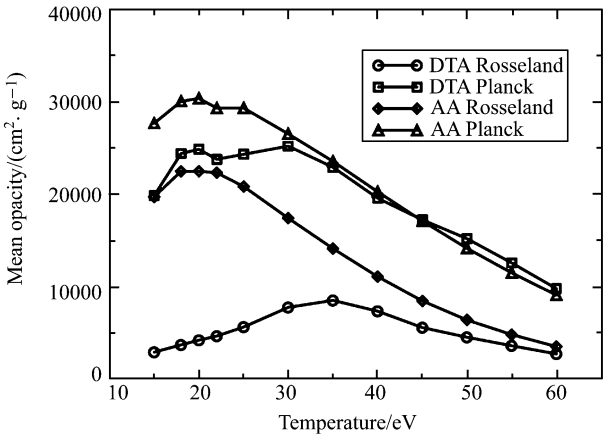

Fig. 12 The Rosseland and Planck mean opacities for aluminum plasmas as a function of temperature at a density of 0.01 g · cm^{-3}.

3.1.5 Opacities of the Z ~ 7.13 sequence*

Under the plasma condition of 40 eV temperature and 0.01 g · cm^{-3} density, the average ionization degree Z^* is 7.13. This result should be correct and reliable when we compare our results with other theoretical ones. Faussurier *et al*. [43] proposed a method for accounting the various ionization stages of an LTE plasma based on the AA model. The method can also be used to estimate different charge state distribution in the plasma. For an aluminum plasma at a temperature of 40 eV and a mass density of 0.0135 g · cm^{-3}, they calculated the average ionization degree to be $Z^* = 7.036$. Considering the lower density 0.01 g · cm^{-3} rather than 0.0135 g · cm^{-3} in our case, our value of the average ionization degree $Z^* = 7.13$ seems natural. The value 7.13 is a little larger than 7.036 because the density of 0.01 g · cm^{-3} is less than 0.0135 g · cm^{-3}. As a matter of fact, we have also solved the Saha equation for the aluminum plasma at a temperature of 40 eV and a density of 0.0135 g · cm^{-3}. According to our calculation, the average ionization degree is 6.95, which is rather close to the value 7.036 obtained by Faussurier *et al*. [43]. Nevertheless, since Faussurier pointed out that their method predicted an ionization higher than another theoretical result obtained by Kilcrease *et al*. [44], our ionization degree of 6.95 agrees better with that obtained by Kilcrease *et al*. They obtained their results also by solving the Saha equation, but the necessary atomic data for the calculations of the partition functions were obtained from the unresolved transition arrays (UTA) approximation [17, 18]. Therefore, we are confident that our results obtained from solving the Saha equation are correct and reliable.

For the $Z^* \sim 7.13$ sequence, we have considered another three cases: 25.24 eV and 0.0001 g · cm^{-3}, 31.04 eV and 0.001 g · cm^{-3}, and 53.35 eV and 0.1 g · cm^{-3}. Figure 13 shows

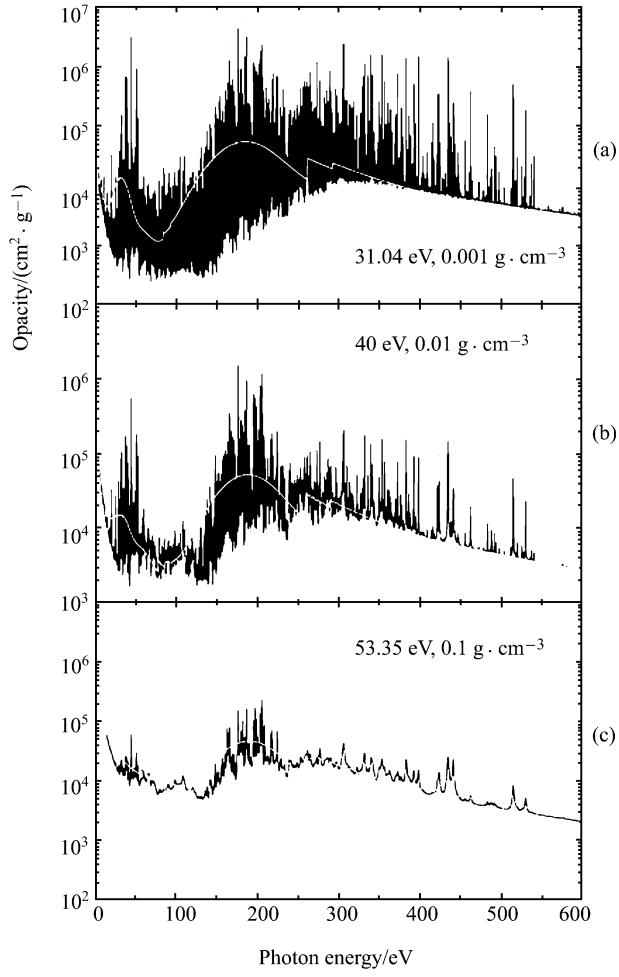

Fig. 13 The spectrally resolved radiative opacities for aluminum plasmas of $Z^* \sim 7.13$ sequence: **(a)** 31.04 eV and 0.001 g · cm^{-3}, **(b)** 40 eV and 0.01 g · cm^{-3} and **(c)** 53.35 eV and 0.1 g · cm^{-3}.

the spectrally resolved opacities of this $Z^* \sim 7.13$ sequence. The corresponding Rosseland and Planck mean opacities are plotted in Fig. 14 as a function of the density. The different temperatures for this sequence are shown at the top of the corresponding results. Similar conclusions to those noted for in Fig. 9 can be drawn from the comparison of the spectrally resolved opacities, although the temperatures are different for the present cases.

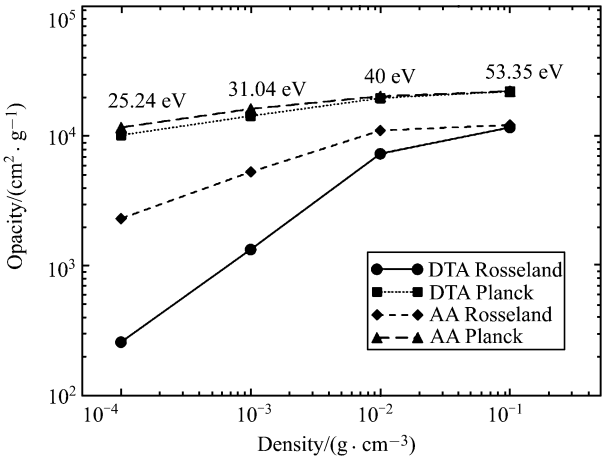

Fig. 14 The Rosseland and Planck mean opacities for aluminum plasmas of $Z^* \sim 7.13$ sequence as a function of density at different temperatures.

3.1.6 Sensitivity to temperature and practical applications

Yang *et al*. [45] measured time integrated transmission spectra of aluminum plasma in the photon energy range of 1730—2060 eV. The absorptions in this region originate from the 1s—*n*p ($n = 3, 4, 5$) photoexcitations of the highly ionized ions of aluminum. Figure 15 shows the theoretical transmission at a density of 0.01 g· cm^{-3} and temperatures of 62, 65 and 68 eV [46]. There are two sets of strong absorptions in the plotted photon energy region. Practical analyses show that the set of 1775—1800 eV are due to the 1s—3p transitions of Al X and the set of 1815—1840 eV are due to the 1s—3p absorptions of Al XI. It can be seen that the transmission is very sensitive to temperature, therefore it can be used as temperature diagnostics. The fact that the experimental sample is not in LTE and there is temperature gradient should be the main reason of discrepancies between the theory and the experiment.

3.2 Radiative opacity of Fe and Br plasmas

3.2.1 Radiative opacity of Fe *plasmas below photon energy of* 1000 eV

Winhart *et al*. [13, 14] carried out their experiment on iron plasma at a temperature of 22 eV and a density of 0.01 g · cm^{-3}. We [47, 48] simulated this experiment using the DLA model. Figures 16 (a), 16 (b) and 16 (c) show the transmission spectra at temperatures of 20, 22 and 24 eV, respectively, in the energy range 70—140 eV, which corresponds to the range measured by the experiments [13, 14]. The solid lines refer to our results obtained by the DLA model while the dashed lines to the experimental results. In Fig. 16 (b), the result obtained by OPAL [49] is also shown with a dotted line. The instrument broadening has been included in all cases. It can be easily seen that the theoretical spectrum obtained best overall agreement with the experiment at a temperature of 22 eV. On the other hand, good agreement is also found below the photon energy of 90 eV at a temperature of 24 eV. This might suggest that the iron plasmas in the experiment are not in strict LTE. It is also noted that the transmission spectra are very sensitive to the temperature. With just 2 eV difference in temperature from case to case, the transmission has obvious difference. This difference is mainly caused by the sensitivity of populations to the temperature. Transmission spectrum can serve as an ideal temperature diagnostic tool because of its sensitivity to the temperature. In the present case, the uncertainty of the theoretical prediction is obviously less than ±2 eV.

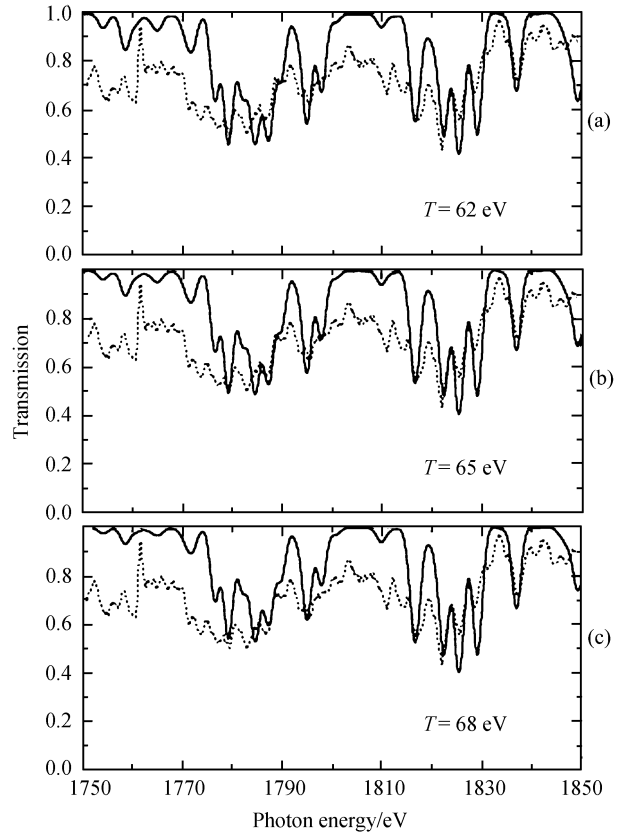

Fig. 15 The temperature diagnostics for the experimental transmission spectrum [45]. The dotted lines in the figures refer to the experimental results and the solid lines to the theoretical results. The temperature in the calculations are 62 eV **(a)**, 65 eV **(b)** and 68 eV **(c)**, respectively. The densities of all calculations are 0.01 g · cm^{-3}. The theoretical results have been systematically shifted 3.1 eV toward the lower photon energy.

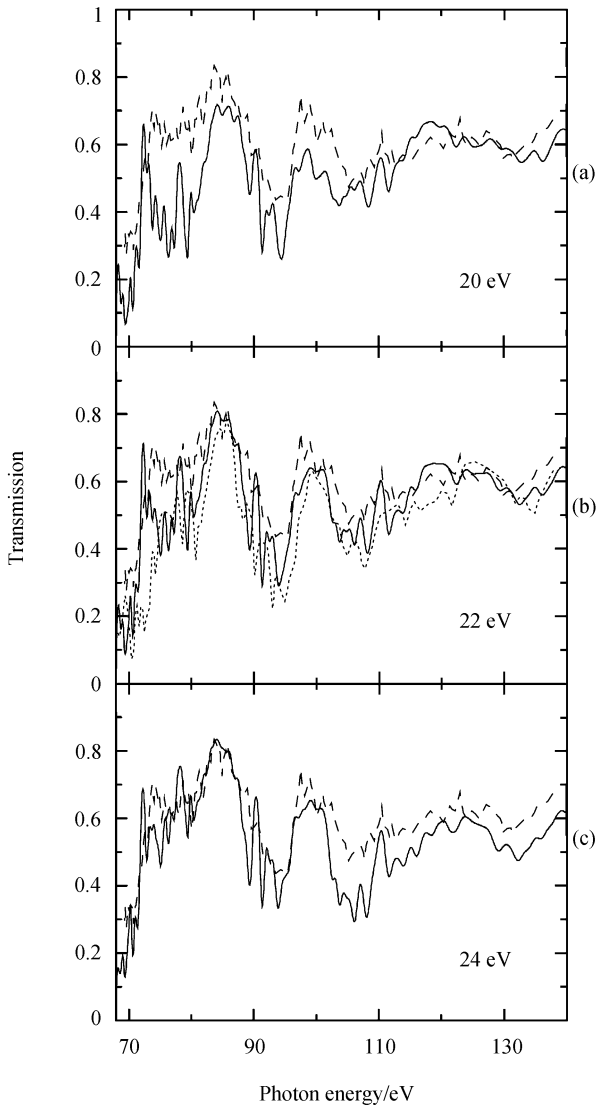

Fig. 16 Transmission as a function of photon energy at temperatures of 20 eV **(a)**, 22 eV **(b)** and 24 eV **(c)**, respectively. The solid lines refer to our results, the dashed ones to the experiment and the dotted one to the OPAL.

OPAL [49] is one of the most accurate code to calculate opacity. From Fig. 16 (b), one can see that our result agrees better with the experiment than does OPAL [49]. The main reason is that we adopt extensive CI wavefunction to obtain the atomic data such as fine-structure energy levels and oscillator strengths, while OPAL performs single configuration Hartree-Fock (HF) calculations to obtain these atomic data. Take also Fe VIII as an example. In addition to all valence electron correlations, the correlations of two 3s and three 3p inner-shell electrons being excited to the 3d orbital are also included in our calculations (full CI). Inclusion of such correlations can considerably decrease the oscillator strengths. In general, the HF method overestimated the oscillator strengths by more than 30 % for the strong transitions, some even more than 70 %.

Springer *et al.* [50] measured transmission of Fe plasma at a temperature of 20 eV and a density of 10^{-4} g·cm^{-3}, which is close to the condition of star envelope. The comparison between our result and the experiment is plotted in Fig. 17. An excellent agreement between the experimental and theoretical results has been achieved. At 82.6 eV and 85.2 eV, both experimental and theoretical spectra have strong absorption, but they are not exactly the same. The experimental absorption at 82.6 eV is much stronger than the DTA result while it is the opposite at 85.2 eV.

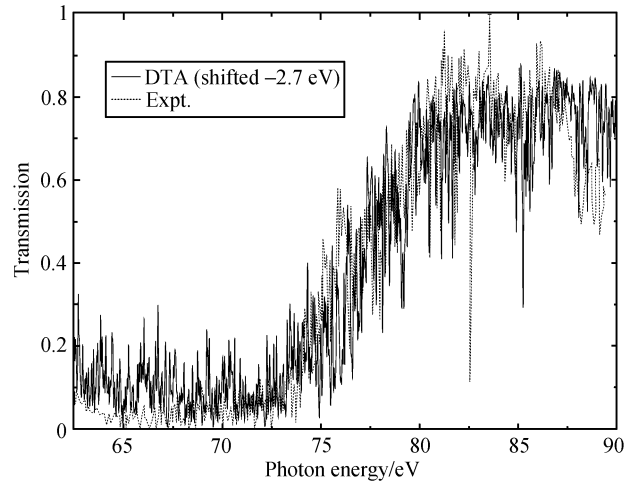

Fig. 17 Comparison between the calculated and experimental [50] transmission of iron plasma at a temperature of 20 eV and a density of 10^{-4} g·cm^{-3}. The dashed line refers to the experiment and the solid line to the theoretical result of DTA.

Because of the importance of Fe plasmas in astrophysics, many theoretical researches [13, 14, 50, 53—55] have been carried out to calculate their opacities at different temperatures and densities. Below the density of 10^{-3} g·cm^{-3}, large disagreement was found among different results. Agreement improves as a density of 0.1 g·cm^{-3} is being reached but then tends to degrade a bit at higher densities. We [48] have calculated an isothermal sequence of iron opacities at the temperature of 20 eV with the density ranging from 10^{-4} to 10^{-2} g·cm^{-3}. The results are shown in Fig. 18. At $T = 20$ eV, the typical Doppler HWHM has an order of 10^{-3} eV. The typical electron impact HWHM is 10^{-1} eV at $\rho = 10^{-2}$ g·cm^{-3}, 10^{-2} eV at $\rho = 10^{-3}$ g·cm^{-3} and 10^{-3} eV at $\rho = 10^{-4}$ g·cm^{-3}. It can be seen that at $\rho = 10^{-2}$ g·cm^{-3}, the lines are so merged together that the spectrum shows a smooth structure, while at $\rho \leqslant 10^{-3}$ g·cm^{-3}, the spectrum is highly resolvable. In this case, the opacity is very sensitive to the individual line width, especially for the Rosseland mean, which should be the main reason of the large difference for different treatment.

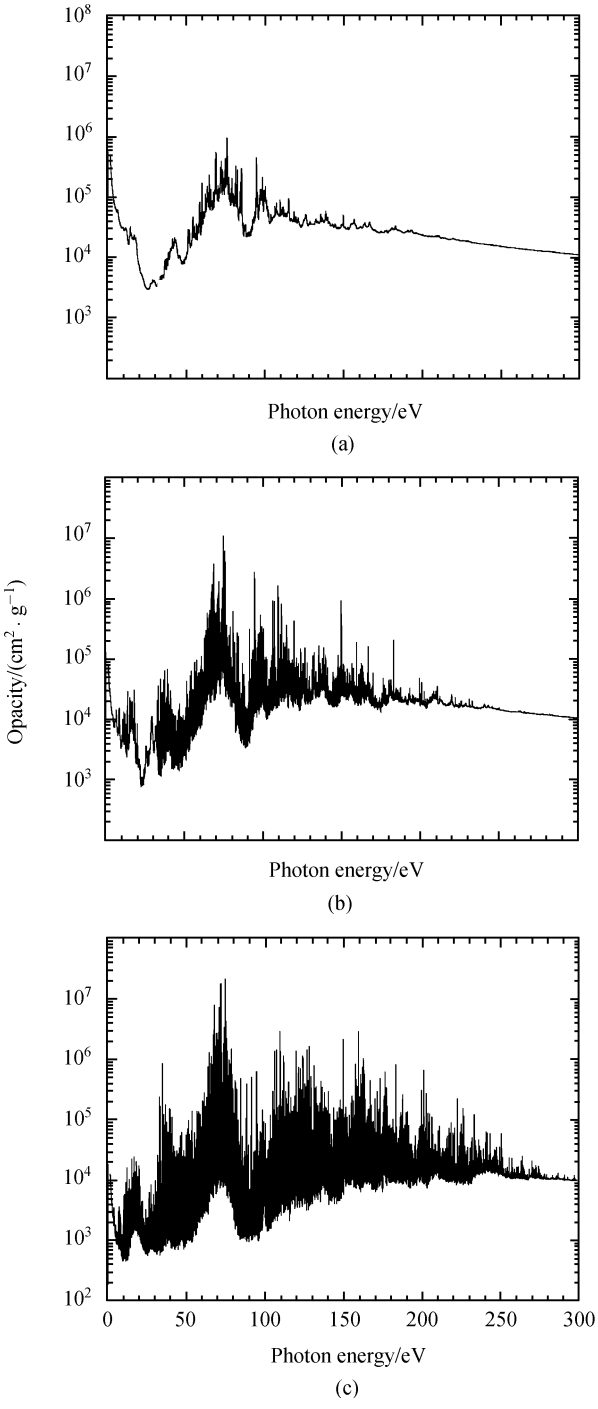

Fig. 18 Spectrally resolved isothermal iron opacities at the temperature of 20 eV and the densities of: **(a)** $\rho = 10^{-2}$ g · cm^{-3}, **(b)** $\rho = 10^{-3}$ g · cm^{-3} and **(c)** $\rho = 10^{-4}$ g · cm^{-3}. The Rosseland and Planck mean opacities are: **(a)** K_R = 21 283 and K_P = 56 624 cm^2 · g^{-1}, **(b)** K_R = 8797 and K_P = 41 258 cm^2 · g^{-1}, **(c)** K_R = 4348 and K_P = 31 185 cm^2 · g^{-1}.

3.2.2 *Transmission of* Fe *plasmas in the* X-*ray region*

For Fe plasmas, many measurements [13, 14, 50, 53—55] are limited to the photon energy region < 300 eV. Chenais-Popovics *et al*. [56] extended the opacity measurement of iron plasmas to a higher photon energy region in the vicinity of 730 eV. The temperature of the plasma is around 20 eV and the areal density is $\rho L = 20$ μg · cm^{-2}. The mass density is estimated to be about 0.004 g · cm^{-3}. Absorption of the 2p—3d transitions of Fe^{4+}-Fe^{9+} has been observed in the experiment. The authors used the super-transition array codes SCO [57] and STA [19] and detailed spin-orbit-split arrays (SOSA) calculations [58] to interpret the experimental transmission. The detailed SOSA calculation is based on the unresolved transition array (UTA) formalism developed by Bauche *et al*. [17, 18], where all the lines of a transition array merge into one broad band. However, as the authors pointed out in their paper, the calculated absorptions are much stronger than the experiment. To obtain the measured transmission, the areal density has to be decreased by a factor of 2.7 for the SCO and STA codes and by a factor of 1.7 for SOSA calculation. The large difference between the theory and experiment is beyond the experimental uncertainties caused by any reasons: the influence of second order spectrum, the thickness uncertainty and temporal and spatial inhomogeneity of the foil. As a result, Chenais-Popovics *et al*. [56] suggested that one has to investigate the effect of individual lines in detail to have a better comparison with the experiment.

We [59] first calculated the transmission spectrum of Fe plasma under the prototype experimental condition of Chenais-Popovics *et al*. [56] using a DLA treatment. In this DLA model, we considered all major spectral line broadening mechanisms: natural lifetime broadening (autoionization and radiative lifetime), electron impact and Doppler broadening. The effects of width of individual lines on the transmission are studied in some detail. Figure 19 (a) shows the calculated transmission spectrum for an iron plasma at a temperature of 20 eV and a density of 0.004 g · cm^{-3}. The autoionization width is taken to be a typical value of 140 meV. This spectrum is highly resolved and shows rich spectral line structures. Note that the saturation effect is evident for some strong lines. Davidson *et al*. [7] and Chenais-Popovics *et al*. [60] studied this effect and concluded that the UTA and STA formalisms cannot correctly describe the saturation of the individual lines because they group many lines together and do not represent them individually with an accurate width.

Figure 19 (b) shows a solid line, the transmission with the instrumental broadening effect having been considered. The dot-dashed, long-dashed and dashed lines refer to the results obtained by SOSA, SCO and STA codes, respectively. All theories assume the iron plasma at a temperature of 20 eV and a density of 0.004 g · cm^{-3} except that the STA code takes a temperature of 21 eV. The dotted line in Fig. 19 (b) refers to the experimental spectrum. Good agreement is observed between our calculated transmission and that of SOSA and the two results agree best with the experiment. However, the four theoretical results that use different approximations (DLA,

UTA, and STA) to treat the transitions predict stronger absorption than in the experiment.

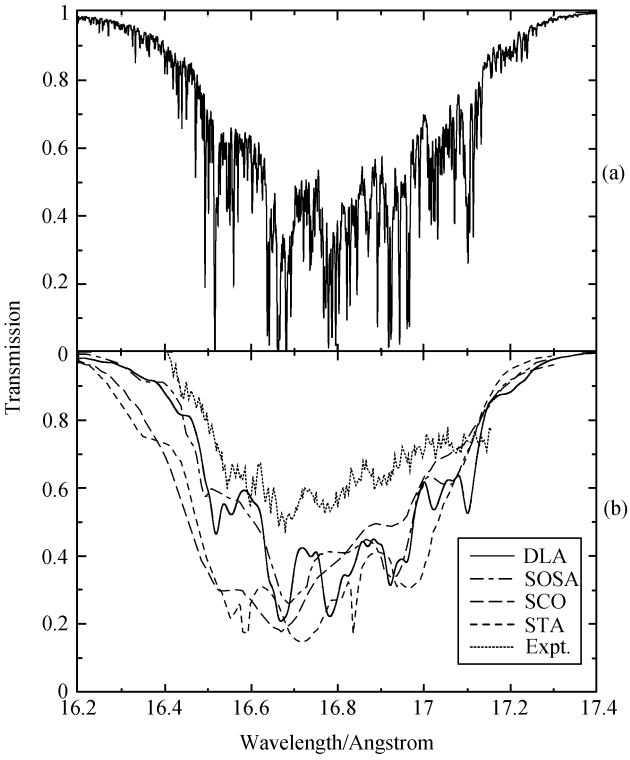

Fig. 19 Transmission calculated as a function of wavelength in Angstrom at a temperature of 20 eV and a density of 0.004 g · cm^{-3}. The autoionization width is taken to be 140 meV for all lines. **(a)** Instrumental broadening not included and **(b)** included.

From the viewpoint of theory, there are several factors which will affect the discrepancy between the DLA theory and the experiment. First, the above calculation used an equivalent autoionization width of 140 meV for all transitions. In fact, for most lines from highly excited levels, the autoionization width is much smaller than 140 meV and the typical value is about 20 meV or less. Using the autoionization widths obtained by FAC code for all transitions, the calculated transmission is shown in Fig. 20 in a solid line. To have a better understanding of the plasma condition, we have also obtained the transmission at temperatures of 18 and 22 eV. From the comparison between the theoretical and experimental transmission, one can conclude that the experimental spectrum has mixed characteristics of the three temperatures. In the short wavelength ward, the temperature of the iron plasma should be between 18 and 20 eV from the DLA results. On the other hand, in the long wavelength range, the temperature seems closer to 22 eV. Therefore, nonhomogeneity of the experimental sample and small temperature gradient existed in the experiment. At the same time, one can see that the transmission is very sensitive to the temperature, which means that it is an ideal diagnostic tool for the temperature of the plasma. The uncertainty of the temperature diagnostics obtained by theoretical predictions should be better than ± 2 eV.

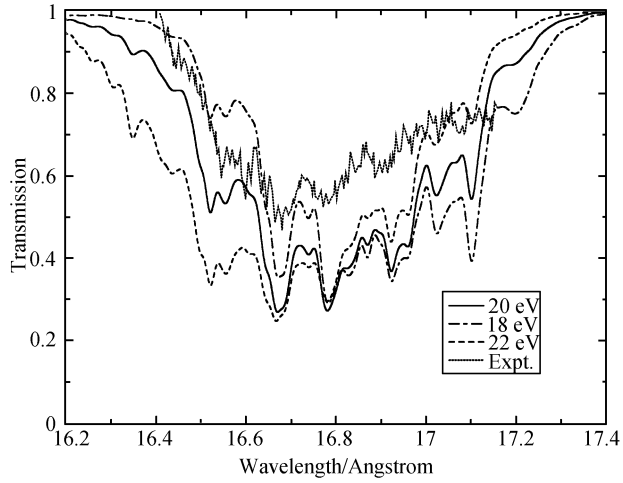

Fig. 20 Transmission at temperatures of 18, 20 and 22 eV with autoionization widths calculated by FAC code for all lines.

The second factor that affects the discrepancy comes from the accuracy of the radiative atomic data. We have carried out a large-scale configuration interaction calculation on the oscillator strengths of Fe VIII within $n < 6$ configurations. Interactions are included among the following configurations: $3s^23p^63d$, $3s^x3p^y3d^z$ ($x + y + z = 9$, $x = 2 - 0$, $y = 5 - 3$), $3s^23p^5 3dnl$, $3s^23p^43d^2nl$, $3s^23p^33d^3nl$, $3s3p^63dnl$, $3s3p^53d^2nl$, $3s3p^4 3d3nl$, $3p^63d^2nl$, $3p^53d^3nl$ ($n = 4, 5$, $l = 0, 1, \cdots, n-1$), as well as all those that can give rise to 2p—*n*d and 2p—*n*s transitions from the above configurations, i.e., $2p^53s^23p + 3d^2$, $2p^53s^x3p^y3d^{z+1}$, etc. The results show that the effect of configuration interaction can generally lower the oscillator strengths by about 20 %. In Fig. 21, the solid line shows the transmission at a temperature of 19 eV after this effect has been included. The dot-dashed line refers to the result obtained by SOSA with individual lines at a temperature of 20 eV and a density of 0.004 g · cm^{-3}. Better agreement is found between both theories of DLA and SOSA with individual lines and the experiment. However, as Chenais-Popovics *et al*. [56] pointed out that the effect of second order reflected by the crystal used in their experiment is estimated to lower the experimental data by 20 %. The dashed line in Fig. 21 shows the result by lowering the transmission by 20 %. After taking account of the second order effect, the agreement is good between the theory and experiment considering the experimental uncertainties mentioned above such as nonhomogeneity of the experimental sample and temperature gradient. From the comparison of Figs. 20 and 21, one can see that the effect of configuration interaction plays a more important role than that of linewidth. No shift is made for the line positions in all our results. Besides good agreement for the overall transmission, very good agreement is also found between the experimental and theoretical line positions. This is an indication of the accuracy of present calculations.

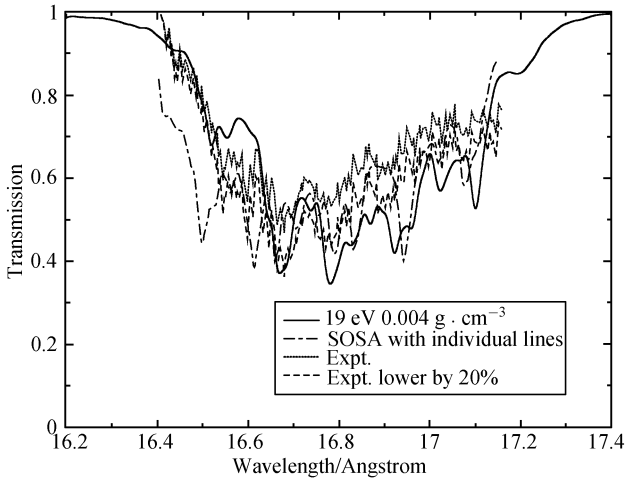

Fig. 21 Transmission at a temperature of 19 eV obtained by further considering the configuration interaction effect. The dot-dashed line refers to result obtained by SOSA with individual lines [56].

3.2.3 *Radiative opacity of* Br *plasmas*

Bailey *et al*. [61] measured the transmission spectrum of NaBr plasma measured in the spectral range of 1450－1900 eV by using the *Z*-pinch radiation at the Sandia National Laboratories *Z* facility. The L to open M shell bromine absorptions were measured in a wide spectral range. We simulated this experiment which is dominated by $n=2$ to $n=3$, 4, and 5 transitions. In their experiment, Bailey *et al*. measured the absorptions of the NaBr sample and took the He δ and He γ lines of the He-like sodium as the detector for the electron density, n_e, from the Stark broadening of the line shapes. An electron density of $(3\pm1)\times10^{21}$cm^{-3} was determined by the best fits to the experimental data. According to the experimental conditions, we took $T=37$ eV and $\rho=0.025$ g·cm^{-3} in our calculation to best fit the measured spectrum in the $2p\rightarrow3d$ absorption. We [62] carried out a detailed study for Br plasmas.

Figure 22 shows the calculated transmission: (a) without considering the instrumental broadening effect and (b) with its effect considered. The structures in the spectral range of 1480－600 eV are due to the open M-shell absorptions, which are caused by the $2p\rightarrow3d$ transitions of the bromine ions. Because of the relativistic splitting of the 2p orbitals, the $2p\rightarrow3d$ absorptions split into two groups. The absorptions around 1517 eV are from the $2p_{3/2}\rightarrow3d_{5/2}$ transitions and the absorptions around 1560 eV from the $2p_{1/2}\rightarrow3d_{3/2}$ transitions.

Figure 23 shows the temperature dependency of the spectrally resolved transmission at the density of 0.025 g·cm^{-3}. The calculated absorptions around 1523 eV and 1564 eV are weaker than the experimental data while the calculated absorptions around 1509 eV is stronger. Figure 23 (b) shows that best fit for the experimental data is obtained when the temperature is chosen to be 37 eV. At this temperature, both the line ratios within the $2p_{3/2}\rightarrow3d_{5/2}$ transition group and the ratio between the two $2p\rightarrow3d$ groups have good agreements with the experiment. When the temperature increases to 38 eV, the absorption at 1523 eV becomes stronger than the experimental data while absorptions at 1509 eV are reduced to be smaller. From Fig. 23 (a) to 23 (c), one can see that a change of 1 eV in temperature can cause perceptible changes in the simulated spectrum, in particular for the relative strength of the absorption structures between 1500 eV and 1530 eV.

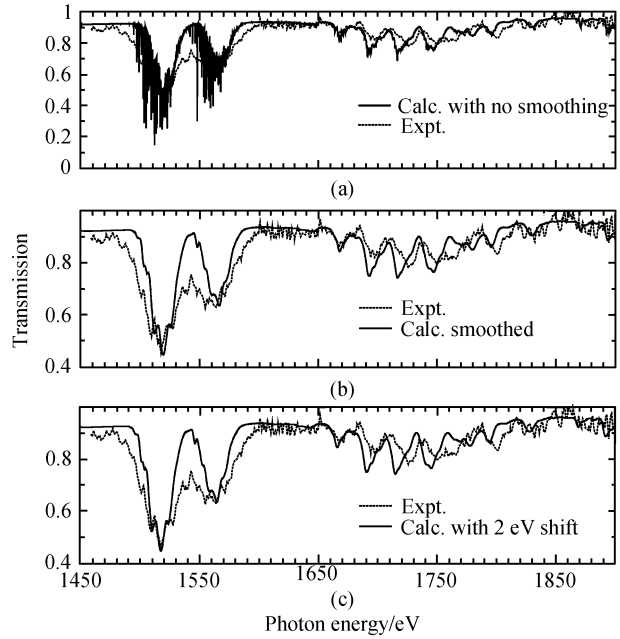

Fig. 22 The radiative transmission of bromine plasma at a temperature of 37 eV and a density of 0.025 g·cm^{-3}. The solid line in **(a)** refers to the theoretical results without convolution with spectral resolution and the dotted line refers to the experimental data. The solid line in **(b)** is the theoretical result, which are smoothed with a width of 1.4 eV according to the instrumental resolution in the experiment. The solid line in **(c)** is the same as that in **(b)** but having a 2 eV shift downward to fit the experimental data.

3.3 Radiative opacity of Au plasmas

For the opacity of light elements such as Al, good agreement is obtained between theory and experiment [8, 20, 63, 64]. For mid- and high-*Z* elements, however, there are systematic discrepancies unexplained so far [24－26]. Are these discrepancies caused by theoretical approximations or experimental uncertainties ? In order to solve this issue, combined efforts from both sides should be made. Experimentally, Iglesias [27] pointed out that unresolved structures in the backlight spectrum can introduce significant errors in the inferred transmission. Theoretically, some physical effects that have been treated approximately or missed in theoretical models may affect the accuracy of opacity. For example, some dis-

crepancies are supposed to be a consequence of line saturation effect [27], which can better be reproduced by detailed level accounting (DLA) models rather than statistical ones. Therefore, it is necessary to investigate the opacity of mid- and high-Z plasmas by using a DLA method, with main physical effects, such as detailed core-valence electron correlation, line saturation and relativity, being considered.

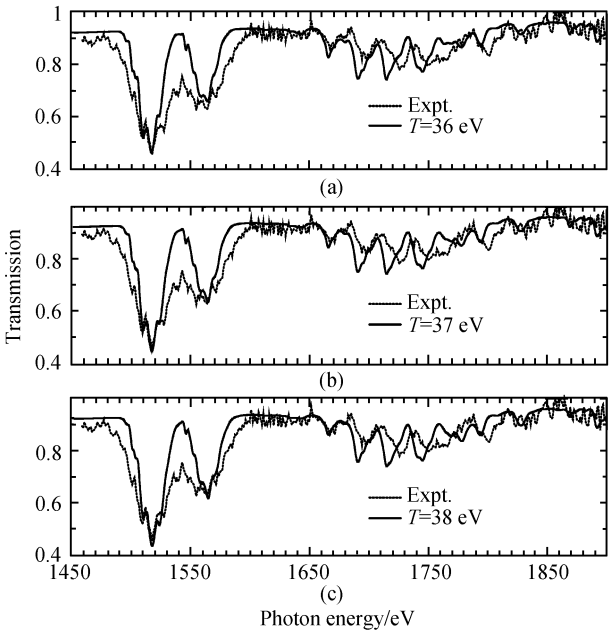

Fig. 23 The temperature dependency of the spectrally resolved transmission at the density of 0.025 g · cm^{-3}. The temperatures in **(a)**, **(b)** and **(c)** are 36, 37 and 38 eV, respectively.

Gold (Au) is an element of particular interest for indirectly driven ICF, where laser radiation heats the inside of a Au hohlraum producing a plasma that emits intense X rays. The X-ray radiation drives the capsule implosion and influences the resulting fusion yield. To design the hohlraum and target, radiative opacity is a crucial physical parameter. Recently, Jones *et al*. [65] measured the absolute albedos of hohlraums from Au or from high-Z mixtures. Their results showed that the albedo of Au predicted by using the opacity of super-transition arrays (STA) agrees better with their experimental values than by using that of an average atom (AA) model. It is generally believed that STA can obtain more accurate opacity than the AA model. Dewald *et al*. [66] carried out the first Au hohlraum experiments at the National Ignition Facility (NIF) using the initial four laser beams to test radiation temperature limits imposed by plasma filling. The NIF project will stress experimental investigation of opacity as one of the most important research fields. So far, some researches have been carried out on the opacity of Au plasmas, both experimentally and theoretically. Eidmann *et al*. [25] measured the opacity of a Au plasma at a density of ~ 0.01 g · cm^{-3} and temperature of~20 eV in a photon energy range of 50 to 300 eV. By mixing appropriate elements with Au, Orzechowski *et al*. [67] experimentally demonstrated the increase of Rosseland mean opacity, which is 1.5 times higher than either of the constituents. Theoretical researches reported in the literatures have used statistical models such as unresolved transition arrays (UTA) [68], STA [25] and AA [69] models. To the best of our knowledge, no work has been reported by using a detailed term accounting (DTA) or DLA model, although such a method is very important to correctly understand and accurately design relevant experiments.

In the following, we investigated the opacity of an Au plasma under the experimental condition of Eidmann *et al*. [25] by using a DLA model. To obtain accurate opacity, one needs accurate atomic data including the energy levels, oscillator strengths, photoionization cross sections, etc. These basic parameters are also important research fields of current work [70, 71]. The atomic data required in the present calculation of opacity are obtained using the Flexible Atomic Code (FAC) developed by Gu [72]. A fully relativistic approach based on the Dirac equation is used throughout the package and thus relativistic effect has naturally been included. Below, we present the effects of core-valence electron correlation and line saturation on the accuracy of opacity. For a Au plasma at a temperature of 22.5 eV and a density of 0.007 g · cm^{-3}, the dominant ion types are Au^{8+}, Au^{9+}, Au^{10+}, Au^{11+}, and Au^{12+}, accounting for 7.6 %, 30.8 %, 34.4 %, 16.2 %, and 9.8 %, respectively.

The effect of core-valence electron correlations can easily be seen from the comparison of Figs. 24 and 25, which show the transmission for a Au plasma under the above plasma condition using different sizes of correlations to calculate the oscillator strengths of bound-bound transitions. In the two figures, the treatment of the bound-free, free-free and scattering processes is the same, while it is different for that of the bound-bound absorption as described below. In Fig. 24, the oscillator strengths of all individual spectral lines have been obtained by considering every necessary transition array one by one for every ion in the plasma. The interactions between all levels generated by all possible couplings within the same configuration have been included. The maximum principle quantum number has been considered up to 12 according to the ionization potential depression. In Fig. 25, however, extensive configuration interactions (CIs) have been included to obtain the oscillator strengths. To illustrate the scale of CIs, we take Au^{11+} as an example. The ground configuration of Au^{11+} is $([Ni]4s^24p^6)4d^{10}4f^{14}5s^25p^6$. The energy of orbitals 5d, 5f, 5g, 6s, 6p, and 6d is relatively low and thus we included them in the expansion of the wavefunction. Large scale CI calculations have been carried out to show its effect. Explicitly, electron correlations have been included among the following configurations: $5p^6$, $5p^5nl$, $5snl$, $4f^{13}nl$, $4d^9nl$, $5p^4n'l'$, $5s5p^5nln'l'$, $4f^{13}5p^55dnl$, $4d^95p^55dnl$, $5p^35d^2nl$, $5s5p^45d^2nl$, $4f^{13}5p^45d^2nl$, and $4f^{12}5p^55d^3$ (nl, $n'l'$ = 5d, 5f, 5g, 6s, 6p, 6d). In the designation, full subshells have been omitted for simplicity. Most of these

correlations are contributed by core-valence electron correlations from the excitations of the 4d, 4f, 5s and/or even 5p core subshells. The remaining oscillator strengths required in the calculation of opacity are treated in the same way as in Fig. 24.

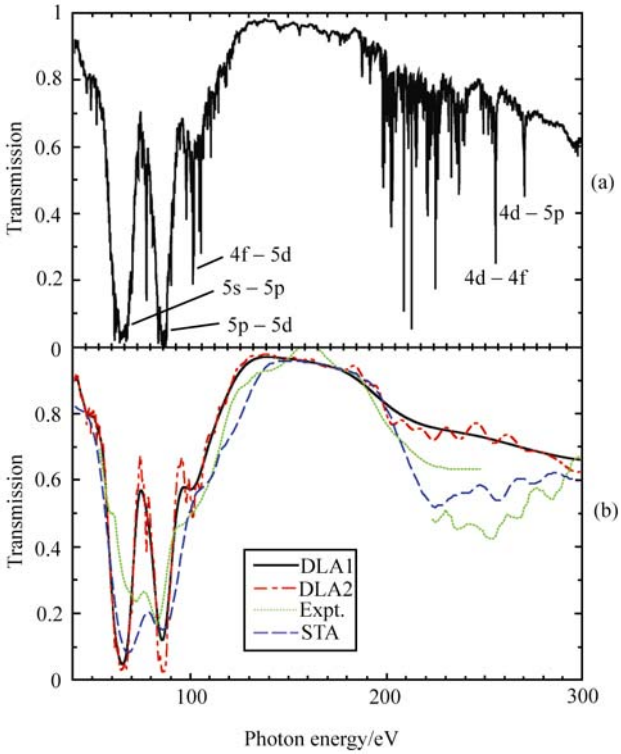

Fig. 24 Transmission of a Au plasma at a temperature of 22.5 eV and a density of 0.007 g · cm^{-3}: **(a)** DLA results and **(b)** instrumental broadening has been included. The experiment and STA data are taken from Ref. [25].

Figures 24 (a) and 25 (a) show our DLA transmission obtained by the two different sizes of correlations described above. The path length L is taken to be 2.5×10^{-5} cm to obtain the results. One can see that the spectrum is highly resolved and shows complex line structures. The line saturation effect is evident for the strong absorption lines. To directly compare with the experiment, one should consider instrumental broadening effect, which can be done by convoluting the DLA transmission over a Gussian function, with full width at half maximum corresponding to the spectrometer resolution. In their experiment, Eidmann *et al*. [25] measured with 1000 and 5000 lines/mm transmission gratings, corresponding to a spectral resolution of 1 nm and 0.2 nm, respectively. In Figs. 24 (b) and 25 (b), the solid line refers to the result of resolution of 1 nm, dot-dashed line to that of 0.2 nm, dotted line to experimental spectrum, and long dashed line to the STA result [25]. We discuss the spectrum in the lower (< 130 eV) and higher (> 200 eV) photon energy ranges, where there are rich spectral line structures.

To begin with, let us pay attention to the two strongest absorption peaks near the photon energy of 70 and 80 eV. In

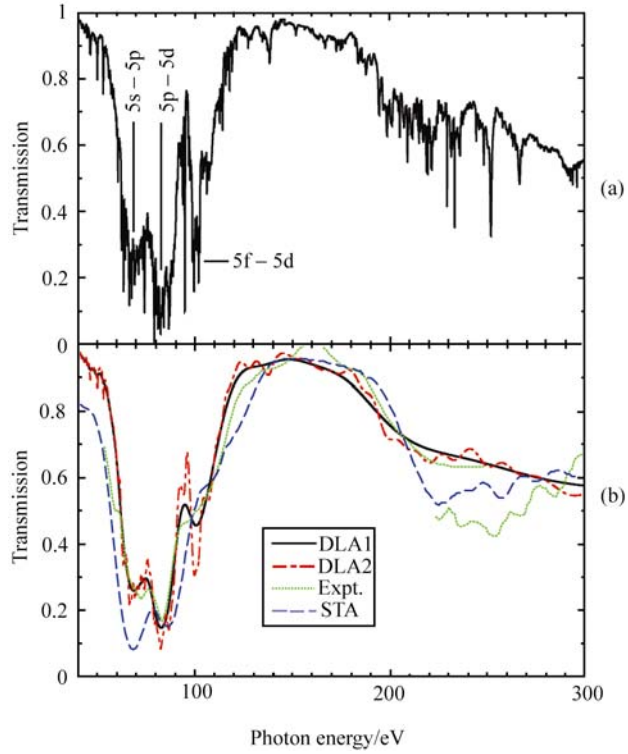

Fig. 25 The same as in Fig. 24, while extensive core-valence electron correlations have been included in the calculation of bound-bound transitions: **(a)** DLA results and **(b)** instrumental broadening has been included. In this figure, the physical effects such as core-valence correlations and autoionization widths have been considered, while in Fig. 24, these effects have not been included.

Fig. 24 (b), the DLA model predicts a larger window than STA in the energy region of 70—80 eV, which is the largest disagreement between the two theoretical results. The relative intensity of the two peaks predicted by both theories is reversed compared with the experiment. The two peaks originate mainly from the absorptions of 5s—5p and 5p—5d transitions, respectively. Both types of transitions have contributions to the two peaks, however, the peak near 70 eV is mainly due to 5s—5p and the other one near 80 eV to 5p—5d. The structures near 100 eV are mainly caused by 4f—5d transitions. When we included extensive core-valence correlations, our DLA transmission is in good agreement with the experiment, not only for the detailed structures, but also for the relative intensity of the two peaks [see Fig. 25 (b)]. The consideration of extensive electron correlations in the bound-bound calculations results in good agreement between our DLA theory and the experiment. The effect of corevalence electron correlations is to lower 5p—5d absorption, but to enhance that of 4f—5d. This effect not only changes the position of the individual lines, but also modifies the distribution of their intensity. Note, however, the small differences in photon energy ranges of 40—60 eV and 110—130 eV between our theory and the experiment, which will be referred to later. Secondly, look at the transmission

above 200 eV. In this energy range, the peaks around 255 eV and 300 eV are mainly due to 4d−4f and 4d−5p absorptions, respectively, although 4f−6g and 4f−7g transitions have contributions as well. Around 200 eV, the structures are mainly caused by 4f−5g transitions. Besides line absorption, contribution of direct photoionization begins to increase with the opening of 4f ionization channel. In this energy region, differences between the DLA results shown in Figs. 24 and 25 are caused by a combined effect of core-valence electron correlation and line width. We have just demonstrated the former effect in detail in the last paragraph; thus we focus our attention to the latter one below. In Fig. 24, we have included the line widths caused by electron impact and Doppler broadening mechanisms. For the lines below 120 eV, this consideration is appropriate, whereas it is not true for the lines above 200 eV, whose upper levels are autoionized states. We have carried out calculations on the autoionization width of some autoionized levels by using Dirac Atomic R-matrix code (DARC) [73]. The results show that a typical value is about 0.4 eV except for the 4d−4f giant resonances, whose width can be more than 1 eV. To simplify the calculation, we take it to be 0.4 eV. The line width caused by electron impact broadening is less than 0.05 eV, while the Doppler width is even smaller. The autoionization width is, therefore, the largest among all broadening mechanisms for these inner-shell transition lines. With the effects of core-valence correlation and line width being considered, our DLA results agree better with the experimental spectrum of resolution of 1 nm.

To have a better understanding of the plasma condition in the experiment, we have also calculated transmission at temperatures of 20 and 25 eV. The results are shown in Fig. 26. One can see that the spectrum is very sensitive to the temperature, both for the overall structures and for the relative intensity of the two strongest peaks. Comparing the theoretical transmission with the experimental spectrum, one can conclude that the experimental spectrum has mixed characteristics of the three temperatures. In the photon energy range of 60−10 eV, the spectrum of 22.5 eV agrees best with the experiment. While below 60 eV, the experimental spectrum has a temperature of 20 eV or even lower. Above the photon energy of 200 eV, the temperature of experimental sample seems to be closer to 25 eV. In the whole photon energy range, the transmission of 22.5 eV agrees best with the experiment. It is evident that nonhomogeneity of the experimental sample and small temperature gradient existed in the experiment [25]. This should be the main reason for the differences between our DLA results and the experiment in the photon energy range of 40−60 eV and 110−130 eV, which has been mentioned above.

The strong sensitivity to the temperature implies that transmission spectrum is an ideal diagnostic tool for the temperature of plasmas. Past experiments have used low-Z materials such as Al as temperature diagnostics (for example, see [74]). Accurate opacity of low-Z materials can be obtained by using a DTA or DLA method. One can deduce the temperature of plasmas by comparing theoretical spectrum with the experiment. However, such a method of tracer element for temperature diagnostics does not always fit for high-Z materials. Because of their complex structures, high-Z elements usually have absorptions over a wide energy range. As a result, they will contaminate the spectrum of tracer element and then affect the accuracy of diagnosis. In this case, transmission spectrum obtained by a DLA model can be used as a tool for temperature diagnostics. The uncertainty should be better than ± 2 eV.

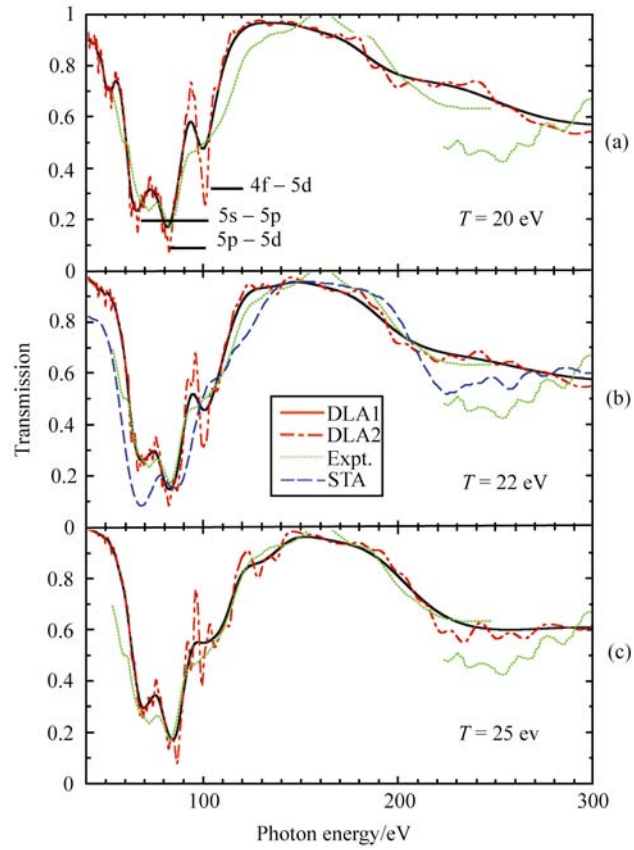

Fig. 26 Transmission of Au plasmas at a density of 0.007 g · cm^{-3} and temperatures of: **(a)** 20 eV, **(b)** 22.5 eV and **(c)** 25 eV, respectively.

3.4 Conclusions

Using our developed DTA and DLA models, we investigated various physical effects on the radiative opacity of different plasmas of low-, medium-, and high-Z elements in LTE. These effects include configuration interaction effect, relativistic effect, and the effect of detailed line width, etc. In the following, we summarize a few key conclusions:

(i) For low-Z aluminum plasmas, in the x-ray region, the importance of the autoionizing widths of the spectral lines of 1s−2p transitions to the convergence of the result with the model size is demonstrated in two ways. The first one treats the 1s−2p transitions approximately as bound-bound proc-

esses and takes the autoionizing effect into account by using a Voigt profile. The second one considers the autoionizing effect more naturally by using a close-coupling *R*-matrix scheme. Both calculations arrive at a good agreement with the experiment and prove that relatively less electron orbitals are required to obtain a converged result in the case that 1s－2p autoionizing resonance broadening is the major broadening mechanism. For higher ionization stages, such as AlX and AlXI, the autoionizing resonance widths are less than the Doppler widths and the convergence of the theory is determined by the Doppler broadening and the relativistic effect.

(ii) For aluminum plasmas, in the EUV region, we calculated the spectrally resolved radiative opacity of Al plasma under a wide range of temperature and density. In particular, we investigated in detail a typical experimental condition at a temperature of 20 eV and a density of 0.01 $g \cdot cm^{-3}$ and compared our results with the experiment. Complex structures, including those caused by bound-bound and bound-free absorptions, dominate the opacity spectrum. All the structures caused by the 2p－3s bound-bound lines are reproduced in our DTA calculation. At the higher photon energies, our DTA transmission exhibits more structures, which also showed up in the experiment, than that of the OPAL. We attribute the good agreement with the experiment at the higher energies to the detailed treatment of the photoionization process. Systematic studies on the spectrally resolved and Rosseland and Planck mean radiative opacities have also been carried out for a 40 eV isothermal sequence, a 0.01 $g \cdot cm^{-3}$ isodense sequence and an average ionization degree $Z^* \sim 7.13$ sequence.

(iii) For medium-*Z* iron plasmas, in the inner-shell transition energy region, the effect of the width of individual lines on the radiative opacity has been studied in detail. The results show that the saturation of the individual lines is evident and important in the detailed transmission calculations. To obtain accurate opacity or transmission, one has to take into account the effect of the width of individual lines caused by all major broadening mechanisms in the plasmas. Considering the experimental uncertainties, reasonably good agreement is obtained between the theory and experiment after the line width effect and configuration interaction effect have been considered in the calculations.

(iv) Also for iron plasmas, in the EUV region, extensive CI wavefunctions are used to calculate accurate atomic data to obtain the radiative opacity. The calculated transmission spectrum is in better agreement with the experiment than do other opacity codes such as OPAL. The transmission is very sensitive to the temperature, as a result, it can be used as temperature diagnostics with the theoretical uncertainty better than ± 2 eV.

(v) For high-*Z* gold (Au) plasmas, various physical effects on the radiative opacity of Au plasmas have been investigated by using the DLA method. The fine treatment for every true individual line by considering the physical effects such as relativity, core-valence electron correlation and autoionization width is essential to reproduce the fine structures of the transmission spectrum of heavy elements, although there are so many individual lines that statistical models can often give reasonable simulations for the general characteristics. Our DLA prediction correctly explained, for the first time, the relative intensity of the two strong peaks due to 5s－5p and 5p－5d absorptions. Above 200 eV, the effect of autoionization width plays a role on the transmission spectrum. The transmission predicted by an accurate DLA method can also serve as a temperature diagnostic tool for high-*Z* plasmas.

In the above, we briefly show some important results obtained by DTA and DLA models. For medium and high-*Z* plasmas, however, there are systematic discrepancies unexplained so far between the theoretical and experimental opacities. Further work is needed to solve the discrepancies, both experimentally and theoretically.

Acknowledgements This work was supported by Program for New Century Excellent Talents in University (NCET), the National Natural Science Foundation of China under Grant Nos. 10474138 and 10204024, the National High-Tech ICF Committee in China, and China Research Association of Atomic and Molecular Data.

References

1. Storm E., Fusion J. Energy, 1988, 7: 131
2. Kauffman R. L., et al., Phys. Rev. Lett., 1994, 73: 2320
3. Rogers F. J. and Iglesias C. A., Science, 1994, 263: 50
4. Iglesias C. A., et al., Astrophys. J., 1995, 445: 855
5. Zeng J. L., Study on the radiative opacity of aluminium plasmas using a model based on the Detailed-Term-Accounting Approximation, Changsha: Press of National University of Defense Technology, 2005
6. Davidson S. J., Foster J. M., Smith C. C., Warburton K. A., and Rose S. J., Appl. Phys. Lett., 1988, 52: 847
7. Davidson S. J., Lewis C. L. S., O'Neill D., Rose S. J., Foster J. M., and Smith C. C., Laser Interaction with Matter edited by Velarde G., Minguez E. and Perlado J. M., Singpore: World Scientific, 1989
8. Perry T. S., Davidson S. J., Serduke F. J. D., Bach D. R., Smith C. C., Foster J. M., Doyas R. J., Ward R. A., Iglesias C. A., Rogers F. J., Abdallah J. Jr., Stewart R. E., Kilkenny J. D., and Lee R. W., Phys. Rev. Lett., 1991, 67: 3784
9. Perry T. S., Ward R. A., Bach D. R., Doyas R. J., Hammel B. A., Phillion D. W., Kornblum H. N., Foster J. M., Rosen P. A., Wallace R. J., and Kilkenny J. D., J. Quant. Spectrosc. Radiat. Transfer, 1994, 51: 273
10. Iglesias C. A., Chen M. H., McWilliams D. L., Nash J. K., and Rogers F. J., J. Quant. Spectrosc. Radiat. Transfer, 1995, 54: 185
11. Foster J. M., Hoarty D. J., Smith C. C., Rosen P. A., Davidson S. J., Rose S. J., Perry T. S., and Serduke F. J. D., Phys. Rev. Lett., 1991, 67: 3255
12. Perry T. S., Springer P. T., Fields D. F., Bach D. R., Serduke F. J. D., Iglesias C. A., Rogers F. J., Nash J. K., Chen M. H., Wilson B. G., Goldstein W. H., Rozsynai B., Ward R. A., Kilkenny J. D., Doyas R.,

Da Silva L. B., Back C. A., Cauble R., Davidson S. J., Foster J. M., Smith C. C., Bar-Shalom A., and Lee R. W., Phys. Rev. E, 1996, 54: 5617
13. Winhart G., Eidmann K., Iglesias C.A., Bar-Shalom A., Minguez E., Rickert A., and Rose S. J., J. Quant. Spectrosc. Radiat. Transfer, 1995, 54: 437
14. Winhart G., Eidmann K., Iglesias C. A., and Bar-Shalom A., Phys. Rev. E, 1996, 53: R1332
15. Kramers H. A., Phil. Mag., 1923, 46: 836
16. Green J. M., J. Quant. Spectrosc. Radiat. Transfer, 1964, 4: 639
17. Bauche-Arnoult C., Bauche J., and Klapisch M., J. Opt. Soc. Am., 1978, 68: 1136
18. Bauche J., Bauche-Arnoult C., and Klapisch M., Adv. At. Mol. Phys., 1987, 23: 131
19. Bar-Shalom A., Oreg J., Goldstein W. H., Shvarts D., and Zigler A., Phys. Rev. A, 1989, 40: 3183
20. Abdallah J. Jr. and Clark R. E. H., J. Appl. Phys., 1991, 69: 23
21. Iglesias C. A., Nash J. K., Chen M. H., and Rogers F. J., J. Quant. Spectrosc. Radiat. Transfer, 1994, 51: 125
22. Zeng J. L., Jin F. T., Yuan J. M., Lu Q. S., and Sun Y. S., Phys. Rev. E, 2000, 62: 7251
23. Berrington K. A., Essner W. B., and Norrington P. H., Comput. Phys. Commun., 1995, 92: 290
24. Perry T. S., et al., J. Quant. Spectrosc. Radiat. Transfer, 1995, 54: 317
25. Eidmann K., Bar-Shalom A., Saemann A., and Winhart G., Europhys. Lett., 1998, 44: 459
26. Iglesias C. A., et al., J. Quant. Spectrosc. Radiat. Transfer, 2003, 81: 227
27. Iglesias C. A., J. Quant. Spectrosc. Radiat. Transfer, 2006, 99: 295
28. Dimitrijevic M. S. and Konjevic N., J. Quant. Spectrosc. Radiat. Transfer, 1980, 24: 451
29. Dimitrijevic M. S., Konjevic N., Astron. Astrophys., 1987, 172: 345
30. Cowan R. D., Theory of Atomic Spectra, Berkeley: University of California Press, 1981
31. Heading D. J., Wark J. S., Bennett G. R., and Lee R. W., J. Quant. Spectrosc. Radiat. Transfer, 1995, 54: 167; and references therein.
32. Yuan J. M., Phys. Rev. E, 2002, 66: 047401
33. Yuan J. M., Chin. Phys. Lett., 2002, 19: 1459
34. Armstrong B. H., Johnston R. R., Kelly P. S., Dewitt H. E., and Brush S. G., Progress in High Temperature Physics and Chemistry, Oxford: Pergamon, 1966, 1: 169
35. Fischer C. F., Comput. Phys. Commun., 1991, 64: 369
36. Zeng J. L., Yuan J. M., and Lu Q. S., Phys. Rev. E, 2001, 64: 066412
37. Zeng J. L. and Yuan J. M., Phys. Rev. E, 2002, 66: 016401
38. Rogers F. J. and Iglesias C.A., Ap. J. Suppl., 1992, 79: 507
39. Rose S. J., J. Phys. B, 1992, 25: 1667
40. Mínguez E., Serrano J. F., and Gámez M. L., Laser Particle Beams, 1988, 6: 265
41. Bar-Shalom A., Oreg J., Goldstein W. H., Shvarts D., and Zigler A., Phys. Rev. A, 1989, 40: 3183
42. Bar-Shalom A., Oreg J., and Goldstein W. H., J. Quant. Spectrosc. Radiat. Transfer, 1994, 51: 27
43. Faussurier G., Blancard C., and Decoster A., Phys. Rev. E, 1997, 56: 3474
44. Kilcrease D. P., Abdallah J. Jr., Keady J. J., and Clark R. E. H., J. Phys. B, 1993, 26: L717
45. Yang J. M., et al., Phys. Plasmas, 2003, 10: 4881
46. Jin F. T., Zeng J. L., and Yuan J. M., Phys. Plasmas, 2004, 11: 4318
47. Zeng J. L., Jin F. T., Zhao G., and Yuan J. M., Chin. Phys. Lett., 2003, 20: 863
48. Jin F. T., Zeng J. L., and Yuan J. M., Phys. Rev. E, 2003, 68: 066401
49. Rogers F. J. and Iglesias C. A., Astrophys. J. Suppl. Ser., 1992, 79: 507
50. Springer P. T., Wong K. L., Iglesias C. A., Hammer J. H., Porter J. L., Toor A., Goldstein W. H., Wilson B. G., Rogers F. J., Deeney C., Dearborn D. S., Bruns C., Emig J., and Stewart R. E., J. Quant. Spectrosc. Radiat. Transfer, 1997, 58: 927
51. Magee N. H., Jr., and Clark R. E. H., see LANL T-4 Opacity Web Page at http://www.t4.lanl.gov
52. Serduke F. J. D., Emilio Minguez, steven J. Davidson, and Carlos A. Iglesias, J. Quant. Spectrosc. Radiat. Transfer, 2000, 65: 527
53. DaSilva L. B., et al., Phys. Rev. Lett., 1992, 69: 438
54. Springer P. T., et al., Phys. Rev. Lett., 1992, 69: 3735
55. Springer P. T., et al., J. Quant. Spectrosc. Radiat. Transfer, 1994, 51: 371
56. Chenais-Popovics C., et al., Astrophys. J. Suppl. Ser., 2000, 127: 275
57. Blenski T., Grimaldi A., and Perrot F., Phys. Rev. E, 1997, 55: R4889
58. Bauche-Arnoult C., Bauche J., and Klapisch M., Phys. Rev. A, 1985, 31: 2248
59. Zeng J. L., Zhao G., and Yuan J. M., Phys. Rev. E, 2004, 70: 027401
60. Chenais-Popovics C., et al., Phys. Rev. A, 1989, 40: 3194
61. Bailey J. E., Arnault P., Blenski T., Dejonghe G., Peyrusse O., MacFarlane J. J., Mancini R. C., Cuneo M. E., Nielsen D. S., and Rochau G. A., J. Quant. Spectrosc. Radiat. Transfer, 2003, 81: 31
62. Jin F. T. and Yuan J. M., Phys. Rev. E, 2005, 72: 016404
63. Zeng J. L., Jin F. T., Yuan J. M., and Lu Q. S., Phys. Rev. E, 2000, 62: 7251
64. Iglesias C. A., Nash J. K., Chen M. H., and Rogers F. J., J. Quant. Spectrosc. Radiat. Transfer, 1994, 51: 125
65. Jones O. S., et al., Phys. Rev. Lett., 2004, 93: 065002
66. Dewald E. L., et al., Phys. Rev. Lett., 2005, 95: 215004
67. Orzechowski T. J., et al., Phys. Rev. Lett., 1996, 77: 3545
68. Yan J. and Wu Z. Q., Phys. Rev. E, 2002, 65: 066401
69. Sun Y. S., Meng X. J., and Zheng S. T., Nucl. Sci. Tech., 1997, 8: 6
70. Brandau C., et al., Phys. Rev. Lett., 2003, 91: 073202
71. Dauvergne D., et al., Phys. Rev. Lett., 2003, 90: 153002
72. Gu M. F., Astrophys. J., 2003, 582: 1241
73. Norrington P. H. and Grant I. P., J. Phys. B, 1987, 20: 4869
74. Perry T. S., et al., Phys. Rev. E, 1996, 54L: 5617